AD-A246 481

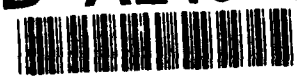

MENTATION PAGE

Form Approved
OMB No. 0704-0188

2. REPORT DATE	3. REPORT TYPE AND DATES COVERED
Feb. 28,1991	Final-8-15-85 to 12-31-88

4. TITLE AND SUBTITLE
Intense Microsecond Electron Beam Interactions with Low-Pressure Gases

5. FUNDING NUMBERS
ONR Contract
SFRC Number
N00014-~~81~~85-K-0542

6. AUTHOR(S)
R. M. Gilgenbach
M. L. Brake

7. PERFORMING ORGANIZATION NAME(S) AND ADDRESS(ES)
Nuclear Engineering Department
University of Michigan
Ann Arbor, MI 48109-2104

8. PERFORMING ORGANIZATION REPORT NUMBER

9. SPONSORING/MONITORING AGENCY NAME(S) AND ADDRESS(ES)
Strategic Defense Initiative--IST
Office of Naval Research

10. SPONSORING/MONITORING AGENCY REPORT NUMBER

11. SUPPLEMENTARY NOTES

12a. DISTRIBUTION/AVAILABILITY STATEMENT
Approved for public release;
distribution is unlimited.

12b. DISTRIBUTION CO

13. ABSTRACT *(Maximum 200 words)*

The major purpose of this project was to examine the ultra-violet to visible emission spectra produced by intense, relativistic long pulse electron beam interactions with gas and plasma environments. Two electron beam accelerators were used in the interaction experiments. The first was MELBA (Michigan Electron Long Beam Accelerator) which operates at the following parameters: Pulselength=1 to 4 μs, Voltage=-0.7 to -1.0 MV; current=1 - 30 kA. A second electron generator (Febetron) with long-pulse modules was also employed: pulselength=0.4 μs fullwidth; voltage=- 0.3 to -0.5 MV; current=1.4 kA.

State of the art optical diagnostics were used to examine the ultra-violet to visible radiation produced by the interaction of the electron beam with gases and plasmas. The two types of gases studied were rare gases (helium, neon, argon, krypton and xenon) and air mixtures (either nitrogen or dry bottled air). The spectrum was measured by either: 1) a low resolution (0.275 meter) spectrograph or a high resolution (1 meter) spectrograph and an intensified optical multichannel analyzer or a photomultiplier tube. The emission spectroscopy studies concentrated on identification of the spectral lines from 180 to 800 nm.Various plasma parameters were determined from the optical emission.

14. SUBJECT TERMS
(25) Electron beams, e-beam-plasma, PLASMA DIAGNOSTICS

15. NUMBER OF PAGES

16. PRICE CODE

17. SECURITY CLASSIFICATION OF REPORT	18. SECURITY CLASSIFICATION OF THIS PAGE	19. SECURITY CLASSIFICATION OF ABSTRACT	20. LIMITATION OF ABSTRACT
UNCLASSIFIED	UNCLASSIFIED	UNCLASSIFIED	

Final Report for Office of Naval Research

Contract Number N00014-85-K-0542

funded by Strategic Defense Initiative IST Program

for Period between August 15, 1985 through December 31, 1988

Project Title: "Intense Microsecond Electron Beam Interactions with Low Pressure Gases"

Principal Investigator: Ronald M. Gilgenbach

Co-PIs: M. L. Brake and T. Kammash

The major purpose of this project was to examine the ultra-violet to visible emission spectra produced by intense, relativistic long pulse electron beam interactions with gas and plasma environments.

Two electron beam accelerators were used in the interaction experiments. The first was MELBA (Michigan Electron Long Beam Accelerator) which operates at the following parameters:

Electron beam Pulselength: 1 to 4 microseconds

Beam Voltage: -0.7 to -1.0 MV

Beam Current: 1 - 30 kA, and

Energy per Pulse: 10 - 20 kJ

A second electron generator (Febetron) with long-pulse modules was also employed:

Beam pulselength: 0.4 microseconds fullwidth,

Beam voltage: - 0.3 to -0.5 MV

Beam current: 1.4 kA

Energy per pulse: ~135 Joules

State of the art optical diagnostics were used to examine the ultra-violet to visible radiation produced by the interaction of the electron beam with gases and plasmas. The light produced was imaged

onto the entrance slit (by means of turning mirrors and lenses) of either 1) a low resolution (0.275 meter) spectrograph or a high resolution (1 meter) spectrograph. The light signal was detected with either an intensified optical multichannel analyzer in gates ranging between 50ns and 4 μs or a photomultiplier tube. The emission spectroscopy studies concentrated on identification of the spectral lines from 180 to 800 nm. Various plasma parameters were determined from the optical emission.

The two types of gases studied were rare gases (helium, neon, argon, krypton and xenon) and air mixtures (either nitrogen or dry bottled air). The results of the various studies are summarized below.

Electron Beam-Generated Emissions from Air

Two studies of electron beam interactions with air were made. The first used MELBA to investigate the interaction of intense electron beams with low pressure, 40 to 100 mTorr, air. Light was gathered from a point 45 cm in front of the foil at an angle of 45^{o}. A Faraday cup was also used downstream of the beam to detect propagation. Even though the area of the beam sampled was quite small, the signal to noise was adequate illustrating the fact that optical sensing can be quite sensitive.

The two major factors in determining the amount of light observed were the pressure of the gas and the amount of e-beam current propagation. Basically, both increased pressure and increased propagation resulted in good signal to noise ratio. However propagation generally occurs for a pressure window of 50-500 mTorr and instabilities result as the pressure increases above 100 mTorr. Basically the best optical signatures occurred for pressures between 40 and 75 mTorr. Note that for all pressures the air emission spectra looked similar; The spectra of dry air showed strong emission from the first negative band of N_2^+ ($B^2\Sigma \rightarrow X^2\Sigma$). Atomic neutral and ion lines were never observed, nor were

impurities such as hydrogen or oxygen.

The second set of studies were performed using the Febetron. The pressures of these experiments ranged from about 1 Torr to 100 Torr. The spectra looked similar to the low pressure cases observed with MELBA but strong emission from the second positive band of neutral N_2 ($C^3\Pi$->$B^3\Pi$) were also observed. Again no other components of air (including atomic nitrogen) were detected.

The vibrational temperatures of the observed vibrational bands were determined from molecular Boltzmann plots to be about 0.33 eV for the N_2 emission and 0.15 eV for the N_2^+ emission. These temperatures fall between the electron temperature of 1 - 2 eV estimated from the rare gas atomic Boltzmann plots (discussed below) and the gas temperature of 0.025 eV estimated from heating and thermal equilibration calculations. The vibrational temperature is not necessarily equal to the electron temperature because vibrational populations require more collisions to equilibrate than do free electron populations. The vibrational temperature is smaller than the plasma electron temperature because the massive nitrogen atoms resist strong vibrations, but is larger than the gas temperature because the plasma does transfer energy to the molecule's vibrational mode.

Note that studies were also made of purely microwave excited air discharges in an attempt to distinguish the optical emission due to the electron beam alone and the microwaves generated by the beam. The optical emission of microwave (2.45 GHz) discharges was similar to the electron beam produced discharges in that emission from N_2 was observed with the absence of atomic lines. In the case of the pure microwave discharges however, the N_2^+ lines were much lower in intensity than the electron beam produced discharges leading to the conclusion that the electron density of the e-beam discharges was much higher. In addition, a

long lived continuum (~ 1 second) was observed in the microwave discharge due to NO recombination with O atoms. The vibrational temperatures obtained were slightly higher than the e-beam plasma alone. They ranged from 0.3 to 0.7 eV for the N_2 emission. Basically the major difference in distinguishing the electron beam produced optical emission and microwave produced optical emission was the NO_2 afterglow.

Electron Beam-Generated Emissions from Rare Gases

A comprehensive study of optical emission produced by electron beams from the Febetron was made. There were several characteristics which were common to all of the gases studied with the Febetron: 1) In all cases, the light emission fell to zero when the beam pulse ended, in contrast to many REB-pumped plasma experiments where the fluorescence of the decaying plasma is measurable for tens of ns to several μs after the beam ends. This indicates that the beam electrons are very important in the population of excited states in this experiment. 2) The time histories of the plasma showed little variation as the plasma evolved. The relative intensities of the emitted lines were roughly constant over time, indicating that the plasma reached steady state within the first 50 ns of the beam pulse. This is is consistent with heating arguements which indicate that both the beam and return current heating reach steady state after the 50 ns risetime of the beam current. 3) Rare gas excimer emission was not detected due to the subatmospheric pressures used. The VUV excimer laser lines were not examined, but several less prominent visible and ultraviolet lines would have been detected if excimer emission was significant. This is in agreement with the chemical kinetics model which predicts excimer emission to be negligible. Also, unusual molecular emission due to molecular impurities was not observed. 4) All of the rare gases exhibited beam-dominated excitation regimes at low gas pressures

where the intensity of the emitted light was linear with gas pressure. The intensities fell off at pressures above 400 Torr, possibly due to self-absorption of the emitted photons.

The spectra emitted by the rare gases followed a trend that scaled with ionization potential in that singly-ionized lines dominated the spectra of the more weakly-binding gases (Ar, Kr, and Xe), while neutral lines dominated the spectra of the more strongly-binding gases (He and Ne). Doubly-ionized lines were most prevalent in xenon, which has the lowest binding energy of the rare gases, and were not observed in gases lighter than krypton. Rare gas excimer emission was not observed due to the subatmospheric pressures used which inhibited the collisional formation of rare gas molecules. The pressure dependence of the rare gas emission shows intensity to be roughly linear with gas pressure between 25 to 300 Torr. The light intensity falls off about 300-700 Torr, possibly due to self-absorption in the relatively denser plasmas.

The optical emission was modeled by extending the Local Thermodynamic Equilibrium (LTE) model to account for the presence of fast beam electrons. These energetic electrons can populate high-lying energy states far above their expected LTE levels, resulting in intense light emission from these states as they spontaneously decay. Indeed, the beam electrons are almost entirely responsible for the production of excited ionic states in this experiment because the plasma densities of 10^{15} - 10^{16} cm^{-3} calculated for this experiment by Brake and Repetti are too high to populate the rare gas ionic states through normal LTE collisional processes. Assuming that the ionic states are populated via excitation from the neutral ground state in this experiment, it is possible to correct for the beam enhancement and put both ionic and neutral lines on an atomic Boltzmann plot to retrieve the excitation temperature of the plasma.

The excitation temperature equals the plasma electron temperature if the plasma has achieved complete local thermodynamic equilibrium. The plasma densities in this experiment are not large enough to achieve full LTE, but are large enough to achieve partial LTE where the populations of the excited states observed in emission are close to their LTE values. The excitation temperatures obtained by the modified Boltzmann plots fell in the range of 1.5 ± 0.7 eV for the rare gases, increasing as atomic weight decreased.

The most probable reason that the effect of e-beam enhancement has not been reported previously is the unique beam-plasma regime studied in this experiment. The Febetron electron beam was not intense and sprayed out from the anode foil into a 40^{o} half-angle cone as int entered the plasma. The beam-to-plasma density ratio of 10^{-4} to 10^{-6} was very low, reducing the return current and instability heating of the plasma. This kept the plasma secondary electron temperature relatively low at approximately 1 eV, which was not enough to appreciably populate the observed ionic states at the existing plasma densities. Under these conditions, the beam excitation effect was clearly evident in the emission spectra.

Other factors contributed to the unique nature of this expeirment. The 300 ns duration of the electron beam was not long enough for the electrons to appreciably heat the ions, but was long enough to achieve a steady state equilibrium in the plasma. The subatmospheric pressures were low enough to discourage excimer formation but were high enough to achieve partial Local Thermodynamic Equilibrium for the observed transitions and also kept the secondary plasma electron temperature low through increased collisions. The plasmas were optically thin at low to intermediate pressure which precluded consideration of radiative excitation and photon transport. Finally, the optical multichannel

anlayzer allowed examination of a wide range of wavelengths. All of these factors help explain the differences between the optical emission observed herein and the results of other investigations.

Studies of helium made with MELBA at pressure between 75 and 227 mTorr showed emission due only to neutral helium. Electron temperatures estimated from electronic temperatures determined from ratios of line intensities yielded a temperature of about 0.5 eV.

Appendix

Faculty Supported by This Contract

1) R. M. Gilgenbach, Professor

2) T. Kammash, Professor

3) M.L. Brake, Associate Professor

Graduate Students Receiving Support from this Contract

1) J. D. Miller

2) T. Repetti

Postdoctoral Researchers Supported by This Contract

1) R. A. Bosch

Doctoral Dissertations Concerning this Project

1) J. D. Miller, "Transport of Long-Pulse Relativistic Electron Beams in Preformed Channels in the Ion Focus Regime", 1989

2) "Emission Spectroscopy of the Interaction of A long-Pulse Relativistic Electron Beam with Rare Gases and Air", 1989

Publications Partially Supported by This Contact

1) "Transport of Long-Pulse, High-Current, Electron Beams in Preformed Monatomic Plasma Channels in the Ion Focus Regime", J. D. Miller and R. M. Gilgenbach, IEEE Trans. on Plasma Science, **18** 658 (1990)

2) "Transport and Stability of Long-Pulse Relativistic Electron Beams in UV Laser Induced Ion Channels," R. F. Lucey, R. M. Gilgenbach, J. D. Miller, J. E. Tucker, and R. A. Bosch, The Physics of Fluids B, 1 430 (1989).

3) "Propagation of Microsecond Electron Beams in Gases and Excimer Laser-Ionized Channels in the Ion-Focused Regime," R. F. Lucey, R. M.

Gilgenbach, J. E. Tucker, and C. L. Enloe, Laser and Particle Beams, 6 687 (1988).

4) "Undulation of a Magnetized Electron Beam by a Periodic Ion Channel," R. A. Bosch and R. M. Gilgenbach, The Physics of Fluids, 31 3127 (1988).

5) "Current Clamping in Long Pulse Electron Beam-Gas Interactions," with R. A. Bosch, S. W. Bidwell and R. M. Gilgenbach, IEEE Trans. on Plasma Science, 16, 428 (1988).

6) "Influence of Damping on the Ion Hose Instability", R.A. Bosch and R. M. Gilgenbach, The Physics of Fluids, 31, 2006 (1988).

7) "Radial Oscillations and the Ion Hose Instability of an Electron Beam Propagating in a Periodic Ion Channel," R. A. Bosch and R. M. Gilgenbach, The Physics of Fluids, 31, 634 (1988).

8) "Leak Widths Resulting from Plasma Diffusion in a Magnetic Cusp", R.A. Bosch and R. M. Gilgenbach, Physics Letters A, 128, 437, (1988).

9) "Transport and Modulation of Relativistic Electron Beams by Periodic Ion Channels," J. Miller and R. M. Gilgenbach, The Physics of Fluids, 30 3165 (1987).

10) D.B. McGarrah and M.L. Brake, Argon Ion Excitation by Relativistic Electrons: I. Collisions Cross Sections and Deposition Efficiencies", Laser and Particle Beams 8 493 (1990)

11) D.B. McGarrah and M.L. Brake, Argon Ion Excitation by Relativistic Electrons: II. Chemical Kinetics", Laser and Particle Beams 8 507 (1990)

T-PS/18/3//35709

Transport of Long-Pulse, High-Current Electron Beams in Preformed Monatomic Plasma Channels in the Ion Focus Regime

Joel D. Miller
Ronald M. Gilgenbach

Reprinted from
IEEE TRANSACTIONS ON PLASMA SCIENCE
Vol. 18, No. 3, June 1990

Transport of Long-Pulse, High-Current Electron Beams in Preformed Monatomic Plasma Channels in the Ion Focus Regime

JOEL D. MILLER, MEMBER, IEEE, AND RONALD M. GILGENBACH, MEMBER, IEEE

Abstract—**Experiments have been performed demonstrating the efficient transport of long-pulse, high-current electron beams in well-diagnosed, preformed plasma channels. Channels were created by the low-energy electron-beam ionization of low-pressure monatomic gases. These transport efficiencies are comparable to the optimum values obtained for similar pulselengths in previous long-pulse, electron-beam transport experiments in laser-preionized diethylaniline gas. Experimental results show the development of both transverse current centroid oscillations characteristic of the ion hose instability and the microwave emission indicative of relativistic electron beam–plasma electron two-stream instability. Significant microwave emission indicating rapid growth of the two-stream instability has been observed in the *S*-band when the space-charge neutralization fraction f_e exceeds unity.**

I. Introduction

PULSED, high-power relativistic electron-beam (REB) technology has significant applications to advanced accelerators, the generation of high-power microwaves [1], laser excitation [2], and free electron laser development [3]. In particular, recent advances in pulsed power technology [4] have made available electron-beam generators capable of producing high-current REB's of long duration ($> 1\ \mu s$). The benefits to these technologies of large delivered energies (> 10 kJ) using long-pulse electron beams may be significant.

Important to these applications is the stable transport of the electron beam over distances on the order of meters. Stable propagation of high-current REB's in the ion focus regime (IFR) is based on the generation of a well-defined plasma background, created by REB-neutral gas collisional ionization or by preionizing a channel in low-pressure gas; plasma electrons are immediately expelled from the channel by the space charge of the electron beam. The field of the remaining plasma ions reduces the space-charge potential of the electron beam enough to allow the electrostatic repulsive and self-magnetic field forces of the beam to cancel, allowing stable propagation.

Manuscript received September 26, 1989; revised February 14, 1990. This work was partially supported by the Strategic Defense Initiative Office, by the Office of Naval Research, and by the National Science Foundation.

J. D. Miller is with the Naval Surface Warfare Center, Code R42, 10901 New Hampshire Avenue, Silver Spring, MD 20903.

R. M. Gilgenbach is with the Intense Energy Beam Interaction Laboratory, Department of Nuclear Engineering, University of Michigan, Cooley Building, North Campus, Ann Arbor, MI 48109.

IEEE Log Number 9035709.

We present results of experiments to investigate the physics involved in the interaction between a long-pulse high-current REB with preformed IFR plasma channels. The behavior of the electron beam–channel plasma interactions may not be as straightforward as that for short pulse electron beams, since the timescales may now become long enough for the dynamics of the channel ions to become significant.

Short-pulse electron-beam transport in preformed IFR plasma channels was initially investigated elsewhere using channels preformed in organic gases (benzene) [5], [6] by multiphoton UV ionization. Previous experiments at the University of Michigan extended this technique to the investigation of the characteristics of long-pulse ($\approx 1\ \mu s$) electron-beam transport [7], [8] in channels formed using a KrF excimer laser to preionize a channel in diethylaniline (DEA).

Photoionization of organic molecules by UV laser has drawbacks, however [9], for accelerator transport systems. The organic compounds can be difficult to handle, and fragmentation of the large molecules can complicate the channel physics. Additionally, to prevent the channels from becoming overneutralized due to beam-induced ionization during the beam pulse, very low gas pressures and high-power UV lasers are required to ionize the gas to the required level. This is particularly significant for the transport of long-pulse beams.

The experiments reported here utilize low-energy electron impact ionization to overcome the limitations of long-pulse laser guiding. Since electron-impact ionization cross sections are large, the background gas is not restricted to the use of organic molecules, and monatomic background gases may be used which simplify the ion channel physics [10]–[12]. Typically, a weak longitudinal magnetic field (< 100 G) is applied to confine the low-energy electron beam and produce well-defined plasma channels. Since monatomic gases have a relatively long recombination lifetime, the channel ionization can build up over a long period of time (several hundred microseconds) with a very low-current, low-energy beam [10].

II. Plasma Channel Formation

These experiments investigate long-pulse (350 ns) REB propagation in pure-mass monatomic ion channels. Plasma channels have been formed by low-energy elec-

0093-3813/90/0600-0658$01.00 © 1990 IEEE

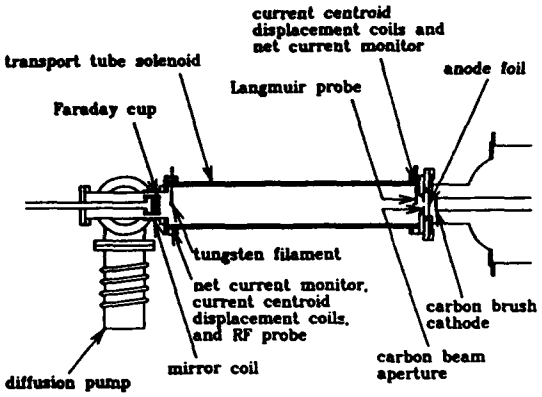

Fig. 1. Experimental configuration for long-pulse REB injection into preionized plasma channels.

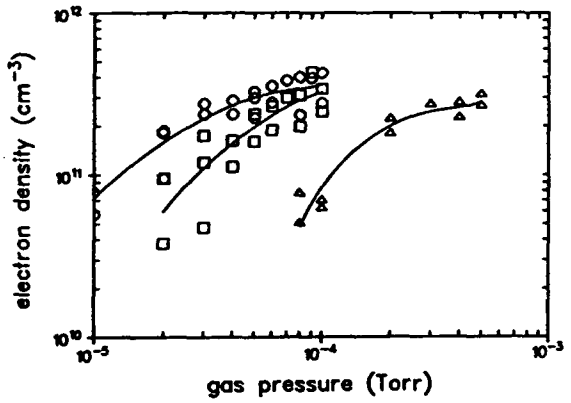

Fig. 2. Channel plasma density on axis 54 cm from the filament versus background gas pressure. Discharge parameters: 800 mA, −300 V, and confining axial magnetic field of 100 G. (△) = neon; (□) = argon; (○) = krypton.

tron impact ionization of noble gases (He, Ne, Ar, Kr, and Xe). The experimental configuration is shown in Fig. 1. The plasma source is a heated tungsten filament on axis, dc-biased to −300 V with respect to the walls of the transport tube (ground). The filament is immersed in the mirror region of a weak (50–100 G) pulsed magnetic field (7-ms risetime). One end of the mirror is matched to the solenoidal field of the transport tube (1-m long, 15-cm diam). The opposite end of the mirror has a larger magnetic mirror ratio to preferentially allow source-plasma electrons to be directed into the transport tube. Axial and radial plasma density profiles have been measured, as well as the temporal evolution of these channels using Langmuir probe techniques. The channel plasma density is adjustable up to about 4×10^{11} cm^{-3} by varying the background gas pressure, the source plasma discharge current, or the confining axial magnetic field. The maximum channel plasma densities obtained in argon, neon, and krypton are shown as a function of gas pressure in Fig. 2. Measurements of the radial channel plasma-density profiles indicate that they are approximately Gaussian with a FWHM radius from 1.0 to 1.5 cm. Axial plasma density measurements indicate uniformity to within 20% down the length of the transport tube for the gas pressures utilized in the experiments.

The channel plasma density is carefully monitored with a Langmuir probe by pulsing the channel separately before injection of the REB. The temporal evolution of the channel plasma density with the confining axial magnetic field is recorded and used to determine the time at which to inject the electron beam on the subsequent pulse. Since the plasma channels have been found to be very reproducible, this provides an accurate determination of the channel plasma density just prior to electron-beam injection.

III. Electron-Beam Injection

Relativistic electron beams are generated by a long-pulse Febetron[1] pulser, operating with the parameters: voltage = −250 to −400 kV; diode current = 1.2 kA; and pulse length = approximately 380 ns. Electron beams are generated from a field-emission cathode-emitting surface consisting of a 2-cm square array of carbon fiber bundles spaced 4-mm apart. This emitting surface is set into a Pierce-type cathode geometry with a diode gap spacing of 2 cm. A 6-μm-thick aluminized Mylar foil separates the diode chamber from the transport region; aluminization is always kept facing the cathode. This thin Mylar foil is used to minimize the scattering of the beam extracted from the diode. After passing through the anode foil the electron beam is apertured by a 1-cm-radius hole in a (1-mm thick) carbon plate located 2-cm downstream from the anode foil. By keeping the aperture diameter at 2 cm, the electrons extracted from the periphery of the cathode-emitting surface, typically with large angular divergence, are scraped-off before injection into the IFR plasma channels. Typical injected beam currents are approximately 200 A.

The carbon aperture plate can be interchanged with a range-thick (1 mm), carbon pinhole mask for characterization of the emittance of the electron beam injected into the transport tube. The pinholes have a 1-mm diam and are placed in a square array 6-mm apart. A 3.2-mm-thick plate-glass Cerenkov imaging screen is located 4-cm downstream from the mask. The diode side of the plate-glass Cerenkov emitter is heavily coated with carbon aerosol (Aerodag) to block the visible light emission from the diode region. The time-integrated Cerenkov light from the beam electrons is viewed through a Lucite window and a plane mirror set at about 45° to the electron-beam axis. Previous experimental evaluation of Cerenkov converters for measuring current density distributions in high-current REB experiments have shown commercial plate glass to have excellent time response and correlation of light output to electron current density [13].

Time-resolved transverse motion of the electron beam is monitored with an array of B_θ-dot (Mirnov) coils [14], [15] located around the circumference of the transport tube. Location of the current centroid (in x–y space) is determined by two pairs of differencing coils (at right angles to each other), together with a measurement of the

[1]Model MIT Pulser, Hewlett-Packard Corp., McMinnville, OR.

net current at the probe location using a Rogowski coil. Two such probes are used in these experiments. One probe, located 3-cm downstream from the carbon aperture plate, provides characterization of the electron beam at injection. The second probe is located 95-cm downstream from the injection point and monitors the behavior of the transported beam.

The transported beam current is measured by a fast rise-time Faraday cup [16] comprised of a vacuum-tight assembly, which is separately evacuated by a dedicated mechanical pump. It measures the transported beam current within 2.54 cm of the axis of the transport tube. A 25.4-μm thick titanium foil discriminates against secondary (plasma) electrons, filtering out electrons below 70-keV energy. The transported electron-beam radial current profile was inferred, with the Faraday cup removed, from the damage pattern observed on a Lucite window at the end of the transport tube.

Radio frequency (RF) and microwave radiation spectra are also monitored to investigate the initiation of streaming instabilities. Input signals are derived from a broadband (single turn) B_θ-dot loop. RF signals are fed to a spectrum analyzer, consisting of an array of bandpass filters and diode detectors, which separates the signal into four frequency bands: 45 to 105 MHz; 138 to 184 MHz; 210 to 265 MHz; and 313 to 373 MHz. Microwave emissions are monitored using a series of successively higher frequency directional couplers and diode detectors. The signal is separated into: *S*-band (2.1–4.3 GHz); *J*-band (4.4–6.6 GHz); *X*-band (6.6–14.2 GHz); *K*-band (14.3–30 GHz); and *Ka*-band (21.1–40 GHz).

The diode region is pumped down to about 2×10^{-5} T by an oil diffusion pump. The transport tube is separately evacuated to a base pressure of about 4×10^{-6} T before backfilling with the desired channel gas. Due to the low background gas pressures required, the diffusion pump on the transport tube pumps continuously. This dynamic-fill technique has proven to be quite reliable and very stable.

IV. Experimental Results and Discussion

Electron-beam transport results have been obtained using pre-ionized, low-density plasma channels preformed in low-pressure neon, argon, krypton, and xenon gas. For the gas pressures utilized in these experiments, relativistic electron impact ionization (Δn_i) is insignificant, since $\Delta n_i / n_{eb} \approx 0.01$ after 350 ns. Beam injection into the transport tube without energizing the tungsten filament resulted in virtually no signal detected from the net current monitor located at the end of the 1-m-long transport tube. This provides confirmation that (a) The background gas pressures are low enough that REB-neutral gas collisional ionization does not play a significant role in channel formation; and (b) the low axial magnetic field used to confine the channel plasma has very little influence on the beam dynamics.

The REB at injection is characterized by a beam current of approximately 200 A with a pulse length of 380 ns. Time-integrated emittance measurements characterizing the beam at injection indicate the initial angular divergence of the beam to be approximately 0.35 rad ($\approx 20°$) on the envelope. The corresponding unnormalized emittance is determined to be approximately 200 cm · mrad. Since the Cerenkov threshold energy in plate glass is approximately 130 keV, these time-integrated emittance estimates represent the first 325 ns of the electron beam pulse.

A. Transport Efficiency

Efficient IFR electron-beam transport is expected to occur for space-charge neutralization fraction values in the range $f_e \geq 1/\gamma^2$ (where f_e is the ratio of the channel ion density to the electron-beam density, $f_e = n_i/n_{eb}$). For a cold (i.e., zero emittance) beam in radial force equilibrium, the IFR condition is $f_e = 1/\gamma^2$, which for these experiments ($\gamma \approx 1.6$) occurs for $f_e \approx 0.4$. In practice, however, values of f_e greater than $1/\gamma^2$ are required to compensate for nonzero beam-emittance effects. Fig. 3 shows a comparison between the transported beam current measured by the Faraday cup (2.54-cm radius) and the transported net current measured by a Rogowski coil (7.5-cm radius) for the channel providing a space-charge neutralization fraction f_e of 0.5. This figure indicates that not all of the beam current transported is collected by the Faraday cup. This result and the corresponding limitations to transport efficiency may be interpreted in terms of the nonzero emittance of the REB.

The equilibrium beam radius of the REB in the IFR plasma channel may be determined from a simple envelope equation analysis [17] as:

$$r_{beq}^2 = \frac{\epsilon^2 I_0 \beta^3 \gamma}{-2I_b (1 - f_e - \beta^2)} \qquad (1)$$

where ϵ is the unnormalized beam emittance, $I_0 = 4\pi\epsilon_0 mc^3/e$, $\beta = v_z/c$, and $\gamma = (1 - \beta^2)^{-1/2}$. For the measured, time-integrated, injected electron-beam emittance of 2.0×10^{-3} m · rad and injected currents of 200 A, the equilibrium beam radius ranges from 3.2 cm for $f_e = 0.5$ to 1.5 cm for $f_e = 1.0$. For f_e values of 0.5, the injected beam relaxes to an equilibrium radius larger than the radius of the collecting surface of the Faraday cup. As a result, not all of the beam current is collected, consistent with the observations. Radial profile measurements inferred from the damage pattern obtained on a Lucite witness plate produced with a space-charge neutralization fraction in argon of 0.9 are in good agreement with the radius predicted by (1). Also consistent with this model is the observation that as f_e approaches unity, the transported beam signal from the Faraday cup and the net current measurement are in very good agreement.

The peak instantaneous current transport efficiency (defined as the ratio of the transported current measured by the Faraday cup to injected current) was as high 76% in these experiments. For long-pulse electron-beam transport, an important figure of merit characterizing the transport technique under investigation is the charge transport

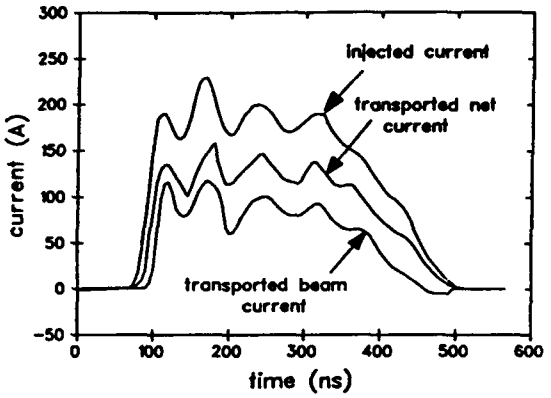

Fig. 3. Comparison of transported beam current (collected in the 2.54-cm radius Faraday cup) and transported net current (collected in the entire transport tube cross section, 7.5-cm radius) to the injected current for $f_e = 0.5$.

efficiency. We define the charge transport efficiency as the ratio of the transported electron-beam charge (as measured by the Faraday cup) to the injected electron-beam charge. Summaries of the experimentally measured peak instantaneous current transport efficiency and charge transport efficiency are shown in Fig. 4(a) and (b). These plots show the transport efficiencies of the preionized plasma channels, in all four gases, for f_e values in the range 0 to 1.6. As expected, current (charge) transport efficiencies greater than 50% (40%) begin around $f_e = 0.35$, in very good agreement with the initial IFR conditions of $1/\gamma^2 \approx 0.4$. The peak current transport efficiency appears to saturate at about 65–70% (peak values of 76%) for f_e values greater than 0.9. Similarly, the charge transport efficiency saturates at about 50% (peak values of 56%) for f_e values greater than 0.75. This limit in transport efficiency is most likely due to the electron beam not being well matched at injection to the equilibrium radius of the REB in the IFR channel.

B. Beam Dynamics

Fig. 5 presents electron-beam transport data for beam injection into an argon channel with a space-charge neutralization fraction $f_e \approx 1.2$. (Note: f_e values greater than unity indicate the presence of excess plasma electrons in the channel that cannot be expelled by the space charge of the REB.) Efficient propagation occurs over the entire pulse length. Peak instantaneous current transport efficiency is 70% for this pulse, while the total fraction of electron-beam charge transported within the Faraday cup diameter was 44%. Plasma current effects, including the return plasma current on the injected net current monitor and possible current multiplication on the downstream net current monitor, were not observed until f_e exceeded 1.2.

Two important features are apparent in the data of Fig. 5. First, the downstream current centroid displacement probe indicates a sinusoidal oscillation in the y (arbitrary) plane. Fig. 6 presents the approximate x–y motion unfolded from the data of Fig. 5. Transverse oscillation of the beam current centroid is clearly illustrated. These results are consistent with the transverse motion of the beam

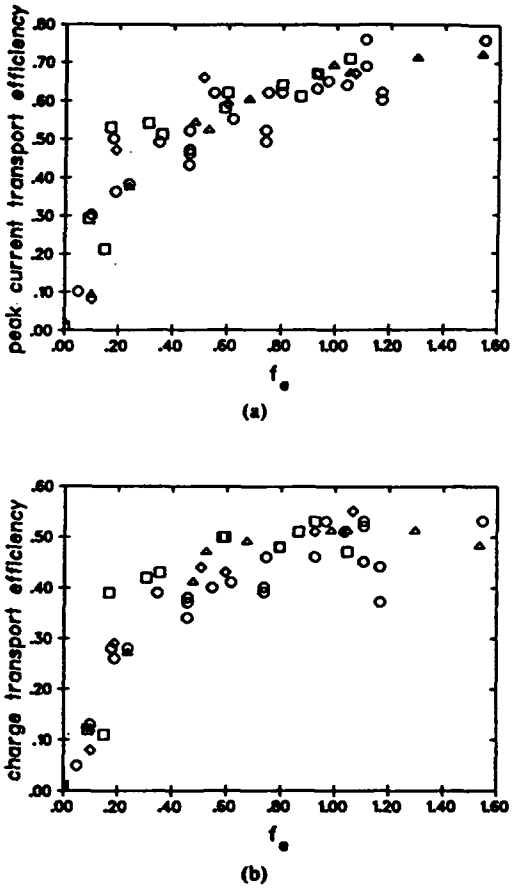

Fig. 4. (a) Peak instantaneous current transport efficiency; and (b) charge transport efficiency versus f_e: (○) = argon at 5×10^{-5} T; (□) = neon at 3×10^{-4} T; (△) = krypton at 5×10^{-5} T; and (◇) = xenon at 3×10^{-5} T.

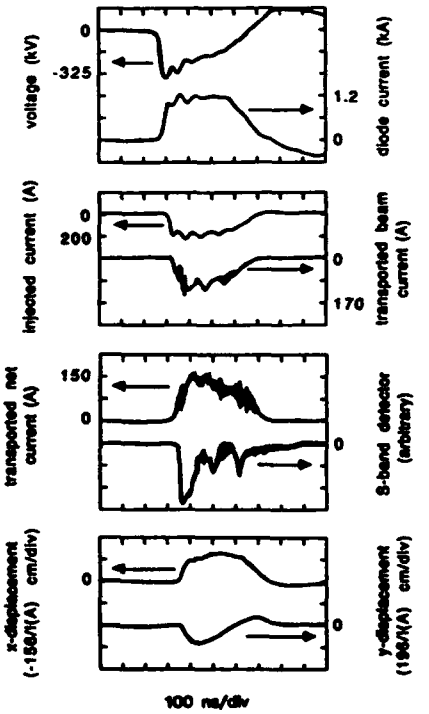

Fig. 5. Experimental data showing transport results for long-pulse electron-beam injection into an argon plasma channel with $f_e = 1.2$. The transported net current monitor is low-pass filtered at 20 MHz.

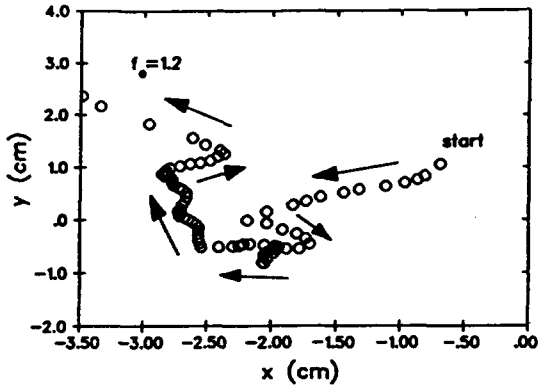

Fig. 6. Unfolded x-y (arbitrary) beam centroid motion from the data of Fig. 5. The data points are spaced 5-ns apart.

due to growth of the ion hose instability [8], [12], [18]–[20]. For these experimental conditions the theoretical frequency for ion hose motion [19] is about 4.6 MHz, which is in reasonable agreement with the experimentally observed oscillation frequency of 2.5 MHz. Data taken over a range of f_e from 0 to 1.6 showed increasing real frequency and maximum excursion with increasing values of f_e. This is qualitatively consistent with the expected scaling [12] of the growth of the ion hose instability ($G \propto f_e^{1/6}$). The development of these oscillations was also investigated as a function of the channel ion mass. Nearly complete oscillations were observed in the neon ($A = 20$ amu) and argon ($A = 40$ amu) data; however, complete oscillations were not observed in krypton ($A = 84$ amu) or xenon ($A = 132$ amu). This scaling with the channel ion mass is also qualitatively as expected for the ion hose instability ($G \propto m_i^{-1/3}$ [12]).

Secondly, examination of the microwave emission signal received by the RF probe in the data of Fig. 5 illustrates a significant frequency component in the S-band. The evolution of the microwave signal with the channel plasma density is shown in Fig. 7(a) and (b). The data shows clear growth of the S-band signal with increasing f_e, becoming significant at $f_e \approx 1.1$. This radiation apparently originates from the REB-plasma electron two-stream instability [21]. This instability can occur when the channel plasma density becomes great enough that excess plasma electrons remain in the channel and interact with the beam electrons. Typically, this streaming instability occurs for f_e greater than unity [6]. For f_e values on the order of 1.2, the electron plasma frequency is approximately 1.3 GHz, near the observed signal frequency range in the S-band. Microwave signals as shown in Figs. 5 and 7 were only observed on the S-band detector. No such signal was obtained for frequencies above 4.3 GHz nor below 343 MHz. No signal was observed in the S-band frequency range for f_e less than 0.8 or 0.9 in any gas.

V. Summary

The data demonstrates that the large value of emittance characterizing the REB at injection requires that space-charge neutralization fractions f_e close to (but less than)

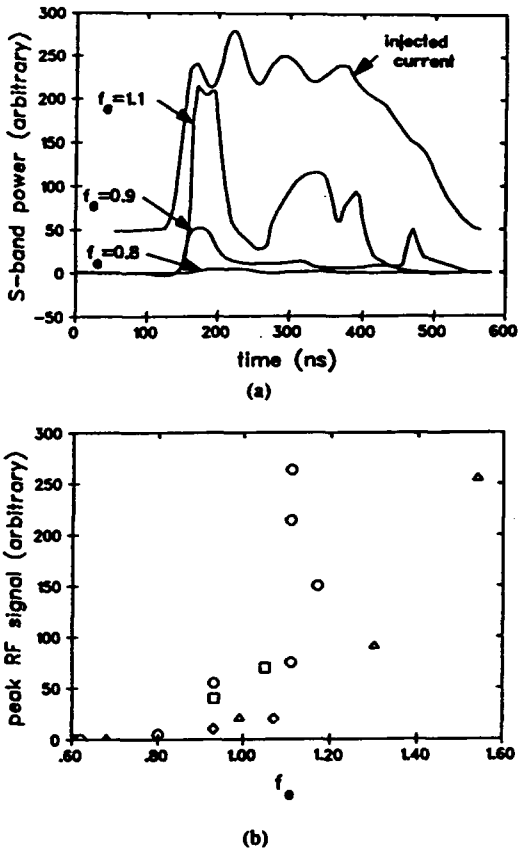

Fig. 7. (a) S-band (2.1–4.3 GHz) microwave output power detected for plasma channels preformed in argon; injected beam-current pulse is shown for comparison. (b) Plot of peak S-band microwave output power versus f_e: (○) = argon at 5×10^{-5} T; (□) = neon at 3×10^{-4} T; (△) = krypton at 5×10^{-5} T; and (◇) = xenon at 3×10^{-5} T.

unity are required to obtain the most efficient electron-beam transport. This limits the maximum instantaneous current transport efficiency to 76% and the charge transport efficiency obtained in these experiments to approximately 56% within the 5.08-cm diam of the Faraday cup. The charge transport efficiency does not appear to be a strong function of the channel gas mass for the present experimental conditions.

Transverse beam centroid oscillations have been observed with real frequencies and qualitative scaling, with f_e and the channel ion mass in agreement with the expected values from the ion hose instability.

The data indicates that the REB-plasma electron two-stream instability can become dominant for measured f_e values as low as 1.1 for our experimental conditions. Transported current signals (Faraday cup) show that the beam current also begins to become strongly modulated when $f_e \approx 1$. This is accompanied by a loss in the transport efficiency and the transported beam energy. Both the charge transport efficiency and transported beam energy peak for f_e values around unity and begin to fall off as f_e is increased further. The initiation of the two-stream instability for f_e values slightly less than unity is likely due to beam electrons interacting with plasma electrons on the periphery of the beam radius.

The results of this study can be compared to our previous experiments concerning electron-beam transport in laser-induced IFR channels utilizing the MELBA electron-beam generator [4] at the parameters: voltage = −0.8 MV; injected beam currents from 200 to 300 A; and pulse lengths variable from 0.4 to 1 μs. In those experiments [8] the background gas pressure was much higher, so electron impact ionization increased the channel ion density during the pulse. The present experiments have operated at background gas pressures low enough that REB-induced electron impact ionization is negligible during the pulse. Peak electron-beam current transport efficiencies in the previous laser ion channel guiding experiments were as high as 80% for comparable pulse lengths, compared to 76% in the present experiments. These experiments demonstrate that ion channel guidance is an effective means of transporting long-pulse, high-current electron beams. However, the neutralization fraction f_e must be kept to less than unity in order to avoid streaming instabilities.

Acknowledgment

One of the authors (JDM) gratefully acknowledges the support of a Rackham Predoctoral Fellowship.

References

[1] Special Issue on High-Power Microwave Generation, *IEEE Trans. Plasma Sci.*, vol. PS-13, Dec. 1985.
Special Issue on High-Power Microwave Generation, *IEEE Trans. Plasma Sci.*, vol. 16, Apr. 1988.

[2] L. A. Rosocha and K. B. Riepe, "Electron-beam sources for pumping large aperture KrF lasers," *Fusion Tech.*, vol. 11, no. 3, pp. 576–611, 1987.

[3] T. C. Marshall, *Free Electron Lasers*. New York: Macmillan, 1985.
C. W. Roberson and P. Sprangle, "A review of free-electron lasers," *Phys. Fluids B*, vol. 1, no. 1, pp. 3–42, 1989.

[4] R. M. Gilgenbach *et al.*, "Microsecond electron beam diode closure experiments," in *Tech. Papers Dig., 5th IEEE Pulsed Power Conf.* (Arlington, VA), 1985, p. 26 (IEEE Cat. No. 85C2121-2).

[5] W. E. Martin, G. J. Caporaso, W. M. Fawley, D. Prosnitz, and A. G. Cole, "Electron-beam guiding and phase-mix damping by a laser-ionized channel," *Phys. Rev. Lett.*, vol. 54, no. 7, pp. 685–688, 1985.
G. J. Caporaso, F. Rainer, W. E. Martin, D. S. Prono, and A. G. Cole, "Laser guiding of electron beams in the ATA," *Phys. Rev. Lett.*, vol. 57, no. 13, pp. 1591–1594, 1986.

[6] R. L. Carlson, S. W. Downey, and D. C. Moir, "Guiding of an electron beam from a *rf* accelerator by a laser-ionized channel," *J. Appl. Phys.*, vol. 61, no. 1, pp. 12–19, 1986.

[7] R. F. Lucey, Jr., R. M. Gilgenbach, J. E. Tucker, and C. L. Enloe, "Propagation of microsecond electron beams in gases and excimer laser-ionized channels in the ion-focused regime," *Laser and Part. Beams*, vol. 6, pt. 4, pp. 687–697, 1988.

[8] R. F. Lucey, Jr., R. M. Gilgenbach, J. D. Miller, J. E. Tucker, and R. A. Bosch, "Transport and stability of long-pulse relativistic electron beams in UV laser-induced ion channels," *Phys. Fluids B*, vol. 1, no. 2, pp. 430–434, 1989.

[9] B. B. Godfrey, B. S. Newberger, L. A. Wright, and M. M. Campbell, "IFR transport in recirculating accelerators," Mission Res. Corp. Final Rep. AMRC-R-741, Nov. 1985.

[10] C. A. Frost, private communication.

[11] J. R. Smith and R. F. Schneider, "Transport of high-brightness electron beams with ion focusing," in *High Brightness Accelerators, Proceedings of a NATO Advanced Study Institute*, A. K. Hyder, M. F. Rose, and A. H. Guenther, Eds. New York: Plenum, 1988, p. 785.

[12] K. J. O'Brien *et al.*, "Experimental observation of ion hose instability," *Phys. Rev. Lett.*, vol. 60, no. 13, pp. 1278–1281, 1988.

[13] G. E. Samlin, "Evaluation of Cerenkov converters for measuring current density distribution in large-area electron beams," *J. Appl. Phys.*, vol. 62, no. 6, pp. 2169–2172, 1987.

[14] S. V. Mirnov, "A probe method for measuring the displacement of the current channel in cylindrical and toroidal discharge vessels," *Plasma Phys. (J. Nucl. Energy Pt. C)*, vol. 7, pp. 325–334, 1965.

[15] C. A. Ekdahl, "Fourier-analyzing coil arrays for pulsed relativistic electron beam experiments," *Rev. Sci. Instrum.*, vol. 55, no. 8, pp. 1221–1228, 1984.

[16] M. A. Greenspan and R. E. Juhala, "Propagation of a 3-ns relativistic electron beam in air," *J. Appl. Phys.*, vol. 57, no. 1, pp. 67–77, 1985.

[17] E. P. Lee and R. K. Cooper, "General envelope equation for cylindrically symmetric charged-particle beams," *Part. Accel.*, vol. 7, pp. 83–95, 1976.

[18] K. J. O'Brien, "Theory of ion hose instability," *J. Appl. Phys.*, vol. 65, no. 1, pp. 9–16, 1989.

[19] R. A. Bosch and R. M. Gilgenbach, "Radial oscillations of an electron beam propagating in a periodic ion channel," *Phys. Fluids*, vol. 31, no. 3, pp. 634–640, 1988.

[20] R. A. Bosch and R. M. Gilgenbach, "The influence of damping on the ion hose instability," *Phys. Fluids*, vol. 31, no. 7, pp. 2006–2008, 1988.

[21] H. S. Uhm, "Two-stream instability in a self-pinched relativistic electron beam," *J. Appl. Phys.*, vol. 56, no. 7, pp. 2041–2046, 1984.

*

Joel D. Miller (S'82–M'89) was born in Cleveland, OH, on February 17, 1960. He received the B.Eng. degree in electrical engineering, and the M.Eng. degree in engineering physics from McMaster University, Hamilton, ON, Can., in 1982 and 1984, respectively. He received the Ph.D. degree (1989) in nuclear engineering from the University of Michigan, Ann Arbor, for experimental and theoretical studies of high-current relativistic electron-beam transport in the ion focus regime.

In 1989 he joined the Directed Energy Technology Branch of the Naval Surface Warfare Center, Silver Spring, MD, where his work involves plasma sources, long-pulse electron-beam generation, and high-current relativistic electron-beam transport.

Dr. Miller is a member of the American Physical Society and the American Nuclear Society.

*

Ronald M. Gilgenbach (S'73–M'74) was born in Fond du Lac, WI, on December 15, 1949. He received the B.S. (1972) and M.S. degrees (1973) in electrical engineering from the University of Wisconsin, Madison. He earned the Ph.D. degree in electrical engineering from Columbia University, New York City, in 1978.

At the University of Wisconsin he was involved in microwave heating of magnetically confined plasmas. His doctoral research at Columbia University concerned high-power microwave generation from intense electron beams. From 1978 through 1980 he was engaged in the gyrotron research program at the Naval Research Laboratory. During the same period, he performed electron-cyclotron heating experiments on the ISX-B tokamak at the Oak Ridge National Laboratory. In 1980 he joined the Nuclear Engineering Department at the University of Michigan, Ann Arbor, where he is currently Professor and Director of the Intense Energy Beam Interaction Laboratory. His research at Michigan concerns long-pulse electron-beam interactions with plasmas and electromagnetic waves, e-beam diode physics, and laser-plasma physics. He is also investigating the industrial applications of lasers, plasmas, and accelerators.

Prof. Gilgenbach is a member of the American Physical Society, the American Nuclear Society, and Sigma Xi.

Laser and Particle Beams (1990), *vol.* 8, *no.* 3, *pp.* 493–506
Printed in the United States of America

Argon ion excitation by relativistic electrons: I. Collision cross sections and deposition efficiencies

By D. B. McGARRAH* AND M. L. BRAKE
Department of Nuclear Engineering, University of Michigan, Ann Arbor, MI 48109, USA

(Received 27 November 1989)

Calculations of the electron impact excitation cross sections and deposition efficiencies for singly ionized argon with electrons of energies up to and including relativistic values have been made using the first Born approximation and the generalized oscillator formalism. Deposition efficiencies for fast electrons were generated from the Peterson and Green integral equation. Cross sections and efficiencies were produced for 29 transitions from the ground state configuration of ArII to excited energy levels with (Ne)$3s^2 3p^4 4s$ and (Ne)$3s^2 3p^4 3d$ configurations and for 40 transitions between excited energy levels from $4s$ and $3d$ to $4p$ orbitals. Efficiencies are constant for electron energies above 1 keV to 10 MeV. Electrons ejected from inner shells contribute up to 12% of the efficiency of the transition for electrons above 10 keV.

1. Introduction

Although relativistic electron beams (REB) are frequently used to pump gas lasers (e.g., Werner *et al.* 1977), the basic understanding of how the fast electrons populate excited states, particularly for ions, is still only approximately known. We have recently observed unusual light emission from REB produced plasmas in rare gases (Brake *et al.* 1986; Brake & Repetti 1988). In order to understand these studies of argon ion emission produced by a relativistic electron beam it is necessary to generate a complete set of cross sections and deposition efficiencies for singly ionized argon experiencing collisions with relativistic electrons.

Peterson and Allen (1971) have calculated efficiencies for certain transitions in argon for neutral atoms experiencing collisions with electrons of energy no more than 10 keV. They used a semiempirical approach based on the Born approximation following the development of Mott and Massey (1965). This assumes that spatial variations are not of interest and uses a continuously slowing down approximation to calculate the energy degradation of the primary electron. More recently, Bretagne *et al.* (1986) investigated collisional excitation of neutral argon due to relativistic electrons. In this paper, the methods of Peterson and Allen (1971) and Bretagne *et al.* (1986) are used to generate the relevant cross sections and efficiencies for singly ionized argon experiencing collisions with electrons ranging in energy from a few eV to 10 MeV.

2. Calculation of electron impact excitation cross sections

A quantum mechanical theory of inelastic collisions of fast charged particles with atoms or molecules was developed by Bethe (1932) using the Born approximation. The relativis-

*D. B. McGarrah's current address is Sandia National Laboratories, Division 8233, Livermore, CA.

 0263-0346/90 $5.00 + .00

tic version of Bethe's differential cross section in generalized oscillator strength formalism for inelastic collisions of electrons with atoms taken from the review by Inokuti (1971) is

$$\frac{d\sigma_{ik}}{d\Omega} = \frac{4e^4}{\hbar^4 c^4} \frac{WW'(k'/k)}{[K^2 - (W - W')^2/\hbar^2 c^2]^2} |\eta_{ik}(K)|^2 \tag{1}$$

where σ_{ik} is the cross section for excitation from level i to level k and Ω is the solid angle subtended by the trajectory of the particle before the collision with that of the trajectory of the incident particle after the collision. W (W') is defined as the total energy of the incident particle before (after) the collision, and k (k') as the wave number of the particle before (after) the collision. The physical constants e, $\hbar$, and c are the charge of an electron, Planck's constant, and the speed of light in a vacuum, respectively. The relativistic form factor η is given by Bretagne *et al.* (1986):

$$|\eta_{ik}(K)|^2 \approx \begin{cases} \dfrac{QF_{ik}(K)}{E_{ik}} & (Ka_0^2) \geq 1 \\ \dfrac{QF_{ik}(K)}{E_{ik}} - \dfrac{(1-\beta^2) f_{ik} E_{ik}}{2mc^2} & (Ka_0^2) \ll 1 \end{cases} \tag{2}$$

where for a relativistic incident particle, Q is defined as follows:

$$Q \equiv \frac{\hbar^2 K^2 - E_{ik}^2/c^2}{2m} \tag{3}$$

and

$$\lim_{k \to 0} F_{ik}(K) = f_{ik} \tag{4}$$

and

$$\mathbf{K} = \mathbf{k} - \mathbf{k}' \tag{5}$$

where $\hbar K$ is the amount of momentum transferred by the collision, $F_{ik}(K)$ is the generalized oscillator strength for the transition from level i to level k and is a function of momentum transfer of the collisional partners, f_{ik} is the optical oscillator strength and is constant for a given transition, E_{ik} is the energy difference between levels i and k, and β is the relativistic beta, i.e., the ratio of the speed of the particle to the speed of light in a vacuum, and m is the mass of the incident particle. The total cross section for collisional excitation can be found by integrating equation (1).

First the differential cross section with respect to solid angle Ω of the change in trajectory of the incident electron is transformed to a differential cross section with respect to the scattering angle θ. Applying the cosine law to the vectors in equation (5) allows transformation of $f(\theta)d\theta$ to $f(K)d(K^2)$. Then the total cross section for collisional excitation can be found by integrating the differential cross section over the limits of possible momentum transfer using the values of the relativistic form factor at the limits of low and high values of (Ka_0^2) as indicated in equation (2). The resulting expression is

$$\sigma_{ik} = \frac{8\pi a_0^2 R^2}{mc^2\beta^2} \frac{f_{ik}}{E_{ik}} \left[\ln\left(\frac{\beta^2}{1-\beta^2} \frac{2mc^2}{R} C_{ik} \right) - \beta^2 \right] \tag{6}$$

where R is the Rydberg energy, a_0 is the Bohr radius, and C_{ik} is a function of the generalized oscillator strengths which in practice is unknown but can be evaluated by experiments. C_{ik} is generally expressed as $\alpha\zeta$ where $\zeta = R/E_{ik}$. Bretagne *et al.* (1986) found that a multiplier of $\alpha = 1/4$ gave good agreement with experimentally measured values for neutral argon. It is assumed that this will hold for argon ions as well (see "Note added in proof").

Since the Born approximation is only valid at high energies, the expression for the excitation cross section must be modified so that it can be used at lower energies. The cross section is modified by defining σ_{ik} equal to B_{ik} times the value of σ_{ik} given in equation (6) where B_{ik} is given as (Bretagne *et al.* 1986):

$$B_{ik} = 1 - \frac{2E_{ik}}{mc^2\beta^2}. \tag{7}$$

To evaluate the excitation cross section it was necessary to obtain values for the energies E_{ik} and the oscillator dipole strengths f_{ik}. Although the energy levels of ArII have been well documented (Moore 1949), it is more difficult to find extensive tables of line strengths for many transitions in ions. Although a few line strengths are known (Wiese *et al.* 1969), a self-consistent set of oscillator line strengths for all transitions of interest had to be generated from an atomic spectra simulation developed by Cowan (1970). The Cowan code consists of a series of three programs. The first generates single configuration radial wavefunctions, the second is an interface program, and the last program performs energy plane wave Born collision-strength calculations. This well-known atomic physics model can be used to produce energy levels and line strengths for all allowed transitions between all energy levels of all given electron configurations from one parity to the opposite parity.

For convenience the cross section, including the modifier from equation (7), will be rewritten in the following form:

$$\sigma_{ik} = \left(A_1 \frac{f_{ik}}{E_{ik}} - A_2 f_{ik}\right)\left[\ln\left(\frac{A_3}{E_{ik}}\right) - A_4\right] \tag{8}$$

with

$$A_1 = \frac{2.55 \times 10^{-19}}{\beta^2}\ [\mathrm{cm^2\ eV}], \tag{9}$$

$$A_2 = \frac{9.96 \times 10^{-25}}{\beta^4}\ [\mathrm{cm^2}]^2, \tag{10}$$

$$A_3 = 1.02 \times 10^6 [\mathrm{eV}]\alpha \frac{\beta^2}{1-\beta^2}, \tag{11}$$

$$A_4 = \beta^2. \tag{12}$$

The parameters E_{ik} and f_{ik} as determined from the Cowan code, are given in table 1 and table 2 for all the transitions that were examined. Measured oscillator strengths compiled by Wiese *et al.* (1969) are also given in table 1 and table 2. Taking into account the fact that the measured oscillator strengths have an error of about 30–50%, there is excellent agreement between the measured values and those generated by the Cowan code.

The cross sections presented in figures 1–4 are calculated using equation (6) multiplied by B_{ik} as given in equation (7) to allow for consideration of low energy as well as relativistic electrons. Note that the cross sections in figures 1 and 2 are for transitions originating from the ground configuration of the argon ion and those in figures 3 and 4 are for transitions beginning from the $(3s^23p^5)\,4s$ configuration, i.e., it is presumed that the level already exists. Only allowed transitions were considered. We have generated cross sections for all transitions listed in table 1 and table 2. The selection rules applied were:

$$\Delta L = \pm 1 \qquad \Delta J = 0, \pm 1 \tag{13}$$

where L is the magnitude of the orbital angular momentum of the ion and J is the magnitude of the total (orbital plus spin) angular momentum. The transitions $3p$–$4s$ and $4s$–$4p$ were chosen to be displayed as they are considered to be significant transitions, for not only

TABLE 1. Energy (E_{ik}) and oscillator line strengths (f_{ik}) for transitions in singly ionized argon between the ground levels with ($3s^2 3p^5$) configuration and the excited levels with configuration ($3s^2 3p^4$) $4s$, $3d$. Whenever possible the line strengths determined from the Cowan code were compared with experimental measurements (Wiese *et al.* 1969).

	Transition	E_{ik}	f_{ik} Cowan	f_{ik} (NBS)
1.	$3p[^2P_{3/2}] - 4s\ [^4P_{5/2}]$	16.43	2.25e-4	
2.	$3p[^2P_{3/2}] - 4s\ [^4P_{3/2}]$	16.53	3.35e-3	2.5e-3
3.	$3p[^2P_{3/2}] - 4s\ [^4P_{1/2}]$	16.59	2.5e-5	1.5e-4
4.	$3p[^2P_{3/2}] - 4s\ [^2P_{3/2}]$	16.91	0.1920	0.18
5.	$3p[^2P_{3/2}] - 4s\ [^2P_{1/2}]$	17.04	0.0404	0.037
6.	$3p[^2P_{3/2}] - 4s'\ [^2D_{3/2}]$	18.30	3.78e-2	
7.	$3p[^2P_{3/2}] - 4s'\ [^2D_{5/2}]$	18.33	0.0004	
8.	$3p[^2P_{3/2}] - 4s'\ [^2S_{1/2}]$	21.16	0.0697	
9.	$3p[^2P_{3/2}] - 3d\ [^2D_{3/2}]$	18.72	0.0738	
10.	$3p[^2P_{3/2}] - 3d\ [^2D_{5/2}]$	18.78	0.1527	
11.	$3p[^2P_{3/2}] - 3d'[^2D_{5/2}]$	21.50	0.5483	
12.	$3p[^2P_{3/2}] - 3d'[^2D_{3/2}]$	21.55	0.1583	
13.	$3p[^2P_{3/2}] - 3d'[^2P_{3/2}]$	21.65	0.2870	
14.	$3p[^2P_{3/2}] - 3d'[^2P_{1/2}]$	21.68	0.4830	
15.	$3p[^2P_{3/2}] - 3d'[^2S_{3/2}]$	22.83	0.4830	
16.	$3p[^2P_{3/2}] - 3d'[^2D_{5/2}]$	22.54	0.0550	
17.	$3p[^2P_{3/2}] - 3d'[^2D_{3/2}]$	22.56	1.15e-3	
18.	$3p[^2P_{1/2}] - 4s\ [^4P_{3/2}]$	16.35	0.0007	9.9e-4
19.	$3p[^2P_{1/2}] - 4s\ [^4P_{1/2}]$	16.42	8.5e-4	6.1e-4
20.	$3p[^2P_{1/2}] - 4s\ [^2P_{3/2}]$	16.74	0.0642	0.072
21.	$3p[^2P_{1/2}] - 4s\ [^2P_{1/2}]$	16.86	0.1464	0.15
22.	$3p[^2P_{1/2}] - 4s'\ [^2D_{3/2}]$	20.98	0.0740	
24.	$3p[^2P_{1/2}] - 4s''[^2S_{1/2}]$	18.54	0.1883	
25.	$3p[^2P_{1/2}] - 3d'[^2D_{3/2}]$	21.38	0.3856	
26.	$3p[^2P_{1/2}] - 3d'[^2P_{3/2}]$	21.48	0.3238	
27.	$3p[^2P_{1/2}] - 3d'[^2P_{1/2}]$	21.51	0.2893	
28.	$3p[^2P_{1/2}] - 3d'[^2S_{1/2}]$	22.81	0.5290	
29.	$3p[^2P_{1/2}] - 3d'[^2D_{3/2}]$	22.38	9.465e-2	

the experimental studies mentioned earlier (Brake *et al.* 1986; Brake & Repetti 1988), but for the general case of transitions in argon ion lasers.

It is difficult to compare the calculated cross sections to experimental values since very little data exists for excited states of argon ions, particularly at relativistic energies. However, a comparison between the calculated values of the excitation cross section and those measured by Feltsan and Povch (1970) for the $4s'$–$4p'$ transition (4277 Å) upon radiative decay from the upper to lower level at low energies is made and shown in figure 5. Unlike experiments examining excitation of neutral argon, it is not possible to directly compare excitation cross sections to experimental measurements for ions since the calculation presumes an initial target of ArII already in a particular energy level which is generally not the case experimentally (most experiments begin with ground state neutral argon atoms). Feltsan and Povch (1970) conducted their experiment by injecting electrons into neutral argon in order to observe transitions in singly ionized argon, that is, they assume a direct, one step ionization and excitation. Our calculations, on the other hand, involve a three step excitation process as follows:

TABLE 2. Energy (E_{ik}) and oscillator line strengths (f_{ik}) for transitions in singly ionized argon between the excited levels with ($3s^23p^5$) $4s$ and $3d$ configuration and the excited levels with configuration ($3s^23p^4$) $4p$. Whenever possible the line strengths determined from the Cowan code were compared with experimental measurements (Wise *et al.* 1969).

	Transition	E_{ik}	f_{ik} Cowan	f_{ik} (NBS)
1.	$4s\ [^4P_{5/2}] - 4p\ [^4P_{3/2}]$	2.521	0.1502	.13
2.	$4s\ [^4P_{3/2}] - 4p\ [^4D_{1/2}]$	2.846	0.0228	0.0165
3.	$4s\ [^4P_{3/2}] - 4p\ [^4P_{3/2}]$	2.419	0.0546	0.0254
4.	$4s\ [^4P_{1/2}] - 4p\ [^4D_{1/2}]$	2.782	0.3439	0.299
5.	$4s\ [^4P_{1/2}] - 4p\ [^4P_{3/2}]$	2.355	0.2024	0.170
6.	$4s\ [^2P_{3/2}] - 4p\ [^2P_{1/2}]$	2.633	0.1517	0.132
7.	$4s\ [^2P_{3/2}] - 4p\ [^2P_{3/2}]$	2.702	0.1610	0.128
8.	$4s\ [^2P_{3/2}] - 4p'\ [^2P_{3/2}]$	4.350	0.0679	
9.	$4s\ [^2P_{1/2}] - 4p\ [^2P_{1/2}]$	2.511	0.0661	0.057
10.	$4s\ [^2P_{1/2}] - 4p\ [^2P_{3/2}]$	2.579	0.4004	0.391
11.	$4s\ [^2P_{1/2}] - 4p'\ [^2P_{3/2}]$	4.227	0.0270	
12.	$4s'\ [^2D_{3/2}] - 4p\ [^2P_{1/2}]$	1.247	0.0279	
13.	$4s'\ [^2D_{3/2}] - 4p'\ [^2D_{3/2}]$	3.099	0.0203	
14.	$4s'\ [^2D_{3/2}] - 4p'\ [^2P_{3/2}]$	2.964	0.0280	0.057
15.	$4s'\ [^2D_{5/2}] - 4p\ [^2P_{3/2}]$	1.281	0.0363	
16.	$4s'\ [^2D_{5/2}] - 4p'\ [^2D_{5/2}]$	3.064	0.1455	0.142
17.	$4s'\ [^2D_{5/2}] - 4p'\ [^2F_{7/2}]$	2.735	0.3968	0.387
18.	$4s'\ [^2D_{5/2}] - 4p'\ [^2P_{3/2}]$	2.928	0.1499	0.18
19.	$4s''\ [^2S_{1/2}] - 4p''\ [^2P_{1/2}]$	1.805	0.2339	0.37
20.	$4s''\ [^2S_{1/2}] - 4p''\ [^2P_{3/2}]$	1.812	0.4693	0.75
21.	$3d\ [^2D_{3/2}] - 4p'\ [^2D_{5/2}]$	2.680	0.0357	
22.	$3d\ [^2D_{3/2}] - 4p'\ [^2P_{3/2}]$	2.545	0.0336	
23.	$3d\ [^2D_{5/2}] - 4p'\ [^2D_{5/2}]$	2.619	0.2615	
24.	$3d\ [^2D_{5/2}] - 4p'\ [^2F_{7/2}]$	2.291	0.1210	
25.	$3d\ [^2D_{5/2}] - 4p'\ [^2P_{3/2}]$	2.484	0.0372	
26.	$3d'\ [^2D_{5/2}] - 4p\ [^2P_{3/2}]$	1.884	0.1508	
27.	$3d'\ [^2D_{5/2}] - 4p'\ [^2P_{3/2}]$	1.903	0.0175	
28.	$3d'\ [^2D_{3/2}] - 4p\ [^2P_{1/2}]$	2.008	0.1044	
29.	$3d'\ [^2D_{3/2}] - 4p\ [^2P_{3/2}]$	1.939	0.0104	
30.	$3d'\ [^2P_{3/2}] - 4p\ [^2P_{3/2}]$	2.042	0.0471	
31.	$3d'\ [^2P_{3/2}] - 4p'\ [^2P_{3/2}]$	0.3942	0.0244	
32.	$3d'\ [^2P_{1/2}] - 4p\ [^2P_{1/2}]$	2.138	0.1638	
33.	$3d'\ [^2P_{1/2}] - 4p'\ [^2P_{3/2}]$	0.4216	0.0111	
34.	$3d'\ [^2S_{1/2}] - 4p\ [^2P_{3/2}]$	8.450	0.0148	
35.	$3d'\ [^2S_{1/2}] - 4p'\ [^2P_{3/2}]$	6.820	0.6865	
36.	$3d'\ [^2S_{1/2}] - 4p''\ [^2P_{3/2}]$	5.094	0.0108	
37.	$3d'\ [^2D_{5/2}] - 4p\ [^2P_{3/2}]$	2.925	0.0626	
38.	$3d'\ [^2D_{3/2}] - 4p''\ [^2P_{3/2}]$	0.4305	0.0327	
39.	$3d'\ [^2D_{3/2}] - 4p\ [^2P_{1/2}]$	3.007	0.0447	
40.	$3d'\ [^2D_{3/2}] - 4p''\ [^2P_{1/2}]$	0.4122	0.0266	

$$e + \text{ArI} \rightarrow \text{ArII}(3p) + e \tag{14}$$

$$e + \text{ArII}(3p) \rightarrow \text{ArII}(4s) + e \tag{15}$$

$$e + \text{ArII}(4s) \rightarrow \text{ArII}(4p) + e \tag{16}$$

followed by radiative decay

$$\text{ArII}(4p) \rightarrow \text{ArII}(4s) + h\nu. \tag{17}$$

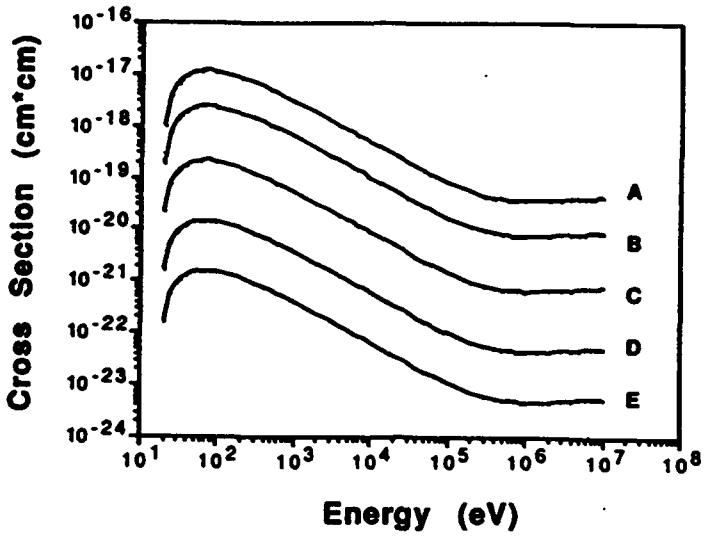

FIGURE 1. Excitation cross sections as a function of electron energy for transitions from the $J = 3/2$ level of the ground configuration ($3s^23p^5$) of ArII to the ($3s^23p^4$) $4s$ configuration where the specific transitions are as follows: $3p[^2P_{3/2}] - 4s[^2P_{3/2}]$ (A); $3p[^2P_{3/2}] - 4s[^2P_{1/2}]$ (B); $3p[^2P_{3/2}] - 4s[^4P_{3/2}]$ (C); $3p[^2P_{3/2}] - 4s[^4P_{5/2}]$ (D); and $3p[^2P_{3/2}] - 4s[^4P_{1/2}]$ (E).

These steps involve the calculation of the probability of ionization and the probability of a transition from level i to level k given a specific i and k being one of the allowed final levels as well as the branching ratios for reaction (17). These various probabilities have been incorporated into the calculated effective cross sections shown in figure 5.

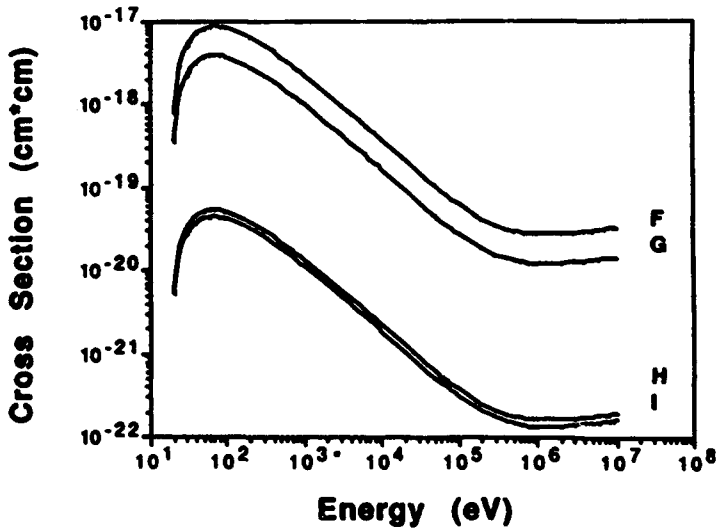

FIGURE 2. Excitation cross sections as a function of electron energy for transitions from the $J = 1/2$ level of the ground configuration ($3s^23p^5$) of ArII to the ($3s^23p^4$)$4s$ configuration, where the specific transitions are as follows: $3p[^2P_{1/2}] - 4s[^2P_{1/2}]$ (F); $3p[^2P_{1/2}] - 4s[^2P_{3/2}]$ (G); $3p[^2P_{1/2}] - 4s[^4P_{1/2}]$ (H); and $3p[^2P_{1/2}] - 4s[^4P_{3/2}]$ (I).

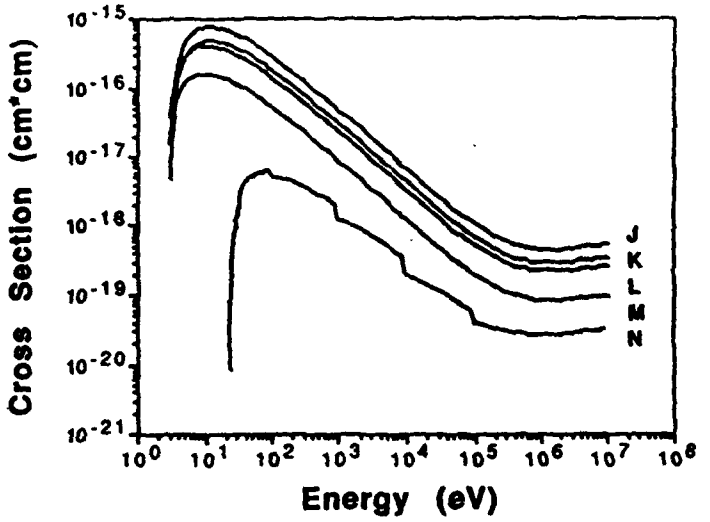

FIGURE 3. Excitation cross sections as a function of electron energy for transitions in ArII from $(3s^23p^5)4s[^4P]$ levels to $(3s^23p^5)4p[^4D,^4P]$ levels where the specific transitions are as follows: $4s[^4P_{1/2}] - 4p[^4D_{1/2}]$ (J); $4s[^4P_{3/2}] - 4p[^4D_{1/2}]$ (K); $4s[^4P_{3/2}] - 4p[^4P_{3/2}]$ (L); $4s[^4P_{3/2}] - 4p[^4P_{3/2}]$ (M); and $4s[^4P_{1/2}] - 4p[^4P_{3/2}]$ (N).

As an additional check, figure 6 shows the low energy calculated cross section for the $4s'$–$4p'$ transition, i.e., equation (16), compared to the common general expression for electron excitation given in plasma formularies (Book 1983):

$$\sigma_{ik} = 2.36 \times 10^{-13} \frac{f_{ik} g(i,k)}{\epsilon \Delta E_{ik}} \text{ [cm}^2\text{]} \tag{18}$$

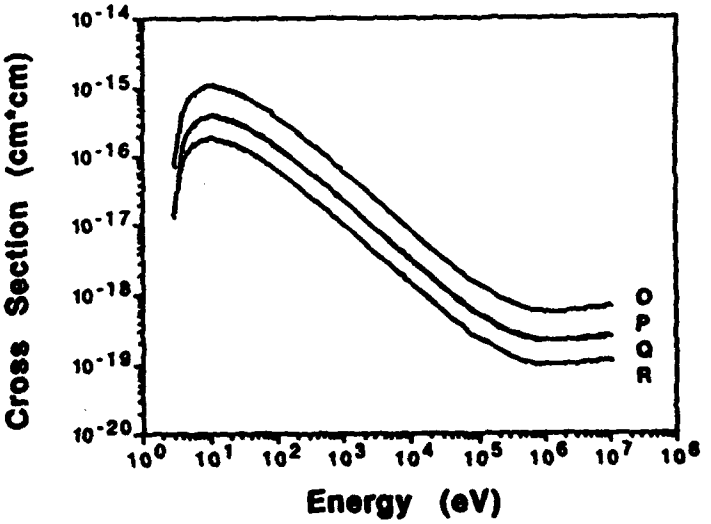

FIGURE 4. Excitation cross sections as a function of electron energy for transitions in ArII from $(3s^23p^5)4s[^2P]$ levels to $(3s^23p^5)4p[^2P]$ levels, where the specific transitions are as follows: $4s[^2P_{1/2}] - 4p[^2P_{3/2}]$ (O); $4s[^2P_{3/2}] - 4p[^2P_{3/2}]$ (P); $4s[^2P_{3/2}] - 4p[^2P_{1/2}]$ (Q); and $4s[^2P_{1/2}] - 4p[^2P_{1/2}]$ (R).

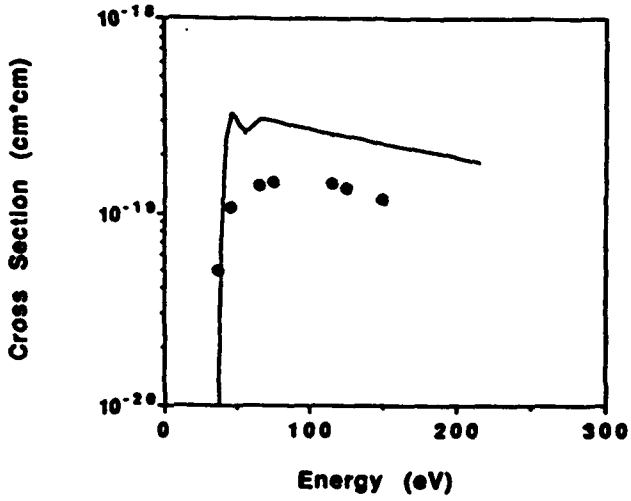

FIGURE 5. Effective excitation cross section for three step process of equations (14)–(16) as a function of electron energy for the $4s' - 4p'$ transition in singly ionized argon (4277 Å). The (•) points indicate the cross section values measured experimentally by Feltsan and Povch (1970).

where f_{ik} and E_{ik} are again the line strength and energy of the transition and here ϵ is the energy of the electron and $g(i,k)$ is the Gaunt factor (generally ~0.2 for ions) (Ono 1980). (Cross sections for other transitions were also compared to their expression and indicated similar agreement.) Note that this approximate expression is inversely proportional to energy and continues to increase to infinity as energy goes to zero. Physically a transition cannot occur for values of energy transfer less than the difference in energy between the upper and lower levels of the transition. Equation (18) thus leads to large errors at values of

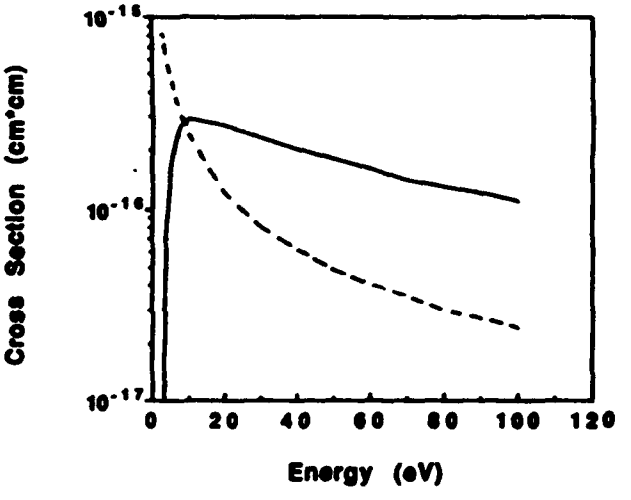

FIGURE 6. Excitation cross section as a function of electron energy for the $4s'$–$4p'$ transition as calculated from equation (8) (smooth line) compared with the cross sections generated from equation (18) (dashed line). Note that the common expression (dashed line) fails at energies near the threshold for the transition.

energy transfer
the relativistic

3. Calculatio

The Peterson
Down Approxi
the number of
of secondary el
k produced by
1968):

with

and

where $N_{ik}(T)$ is
and all subsequ
of transitions i
lower limit is th
a transition fror
tron. The term
energy T_i gener
electron with ki
must be transfe
electron with ki
of the incident
The total loss
atom/ion in en

L_i

It includes both
for low energy

where I_{ij} is the i
shell j. I_{ij} is def
equal to the ion
that level. For i
transitions unde
(in energy) ioniz

energy transfer which are near the threshold for the transition as well as energy levels in the relativistic regime.

3. Calculation of electron beam deposition efficiencies

The Peterson and Green (1968) integral equation based upon the *Continuously Slowing Down Approximation* (CSDA) was used to calculate the energy apportionment. In this way the number of excitations generated by the beam electron and all subsequent generations of secondary electrons can be counted. The number of transitions from energy level i to k produced by a single beam electron with kinetic energy T is given by (Peterson & Green 1968):

$$N_{ik}(T) = N_{ik}^{0}(T) + \sum_{j} \int_{E_{ik}}^{(T-I_{ij})/2} N_{ik}(X) n_{ij}(T,X) dX \tag{19}$$

with

$$N_{ik}^{0}(T) = \int_{E_{ik}}^{T} \frac{\sigma_{ik}(X) dX}{L_i(X)} \tag{20}$$

and

$$n_{ij}(T,T_s) = \int_{2T_s+I_{ij}}^{T} \frac{S_{ij}(X,T_s) dX}{L_i(X)} \tag{21}$$

where $N_{ik}(T)$ is equal to the number of transitions i to k produced by the beam electron and all subsequent generations of electrons generated and $N_{ik}^{0}(T)$ is equal to the number of transitions i to k produced directly by a primary electron with kinetic energy T. The lower limit is the minimum amount of energy that must be transferred to the ion to cause a transition from level i to level k. The upper limit is the kinetic energy of the incident electron. The term $n_{ij}(T,T_s)$ is equal to the number of secondaries per unit energy with kinetic energy T_s generated from ionization of the jth shell of the atom/ion in energy level i by an electron with kinetic energy T. The lower limit is the minimum amount of energy which must be transferred from the incident electron with kinetic energy T to the ion so that an electron with kinetic energy T_s will be ejected. Again, the upper limit is the kinetic energy of the incident electron.

The total loss function for an electron experiencing inelastic scattering off of the target atom/ion in energy i level can be written as (Bretagne *et al.* 1986):

$$L_i(T) = \sum_{k} E_{ik} \sigma_{ik}(T) + \sum_{j} B_{ij} \int_{I_{ij}}^{(T+I_{ij})/2} E \frac{d\sigma_{ij}(T,E)}{dE} dE. \tag{22}$$

It includes both excitation and ionization. Again, modifications have been made to account for low energy electrons with B_{ij} defined as follows:

$$B_{ij} = 1 - \frac{2I_{ij}}{mc^2\beta^2} \tag{23}$$

where I_{ij} is the ionization potential for an atom/ion in energy level i to lose an electron in shell j. I_{ij} is defined in this manner so that, in the valence shell for an excited level, I_{ij} is equal to the ionization potential minus the energy difference between the ground state and that level. For inner shells, the ionization potential remains the same since all excitation transitions under consideration involve valence electrons only. $S_{ij}(T,E)$ is the differential (in energy) ionization cross section for an incident electron with kinetic energy T transfer-

ring energy E to the target atom/ion in energy level i by ejecting an electron from the jth shell. It was calculated as the sum of two terms representing glancing and hard collisions. The glancing collision term is an extension of the differential excitation cross section where the excitation energies are allowed for transitions into continua and is recast from $f(K)d(K^2)$ to the form $f(Q)d(\ln Q)$. The glancing component of the differential ionization cross section is thus:

$$S_{ij}(T,E) = \left.\frac{d\sigma_{ij}(T,E)}{dE}\right|_g = \frac{2\pi e^4}{mc^2\beta^2}\int_{Q_1}^{Q_j}\frac{|\eta_j(K,T)|^2 d|\ln Q|}{Q}. \quad (24)$$

Evaluating the integral and using the result of Bretagne *et al.* (1986) for the lower limit

$$Q_1 = \frac{T^2(1-\beta^2)}{2mc^2\beta^2}. \quad (25)$$

The upper limit on Q, Q_j, for a glancing ionization collision ejecting an electron in the jth shell, is given by Bretagne *et al.* (1986) for neutral argon. They show that $Q_j = 1500$ eV for the K shell, 100 eV for the L shell, and $1.1 + 0.3[1. - \exp(-(E - I_{iM})/5)]$ for the M shell where $I_{iM} = I_M - E_i$. I_M equal to 27.63 eV is the ionization potential of ArII in the M

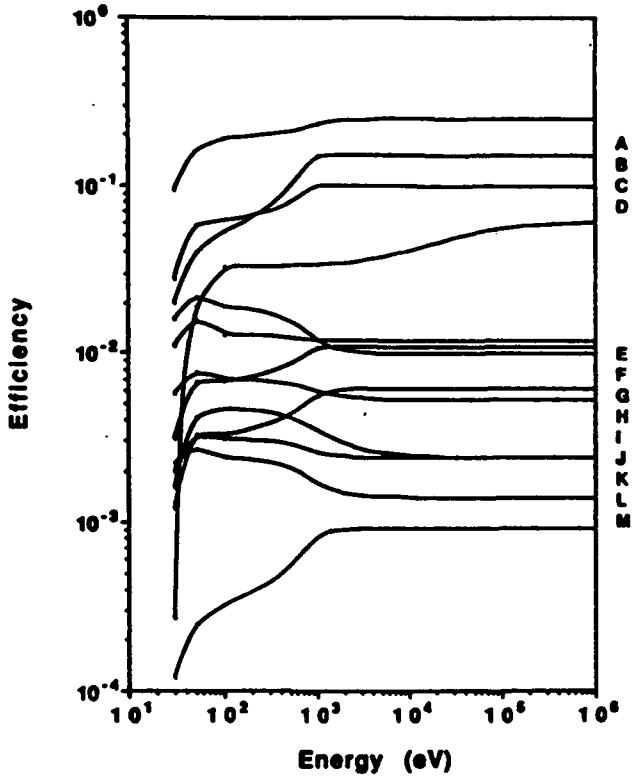

FIGURE 7. Deposition efficiencies of the $(3s^23p^4)$ $4s$ and $3d$ levels originating from the $J = 3/2$ level of the ground configuration $(3s^23p^5)$ of ArII as a fraction of the incident energy where the final states are as follows: $4s[^2P_{3/2}]$ (A); $4s[^4P_{3/2}]$ (B); $3d'[^2D_{5/2}]$ (C); $3d'[^2S_{3/2}]$ (D); $3d'[^2P_{3/2}]$ (E); $3d'[^2P_{1/2}]$ (F); $3d[^2D_{3/2}]$ (G); $4s[^4P_{5/2}]$ (H); $4s[^2P_{1/2}]$ (I); $3d'[^2D_{5/2}]$ (J); $4s'[^2D_{5/2}]$ (K); $3d[^2D_{3/2}]$ (L); $4s[^4P_{1/2}]$ (M).

shell, and E_i is the ith energy level of the ion. The unsubscripted E refers to the energy transferred from the incident electron during the collision. We assume that these limits hold for argon ions, as well as neutrals, if the appropriate ionization potential is used for the M shell of the ion. The glancing component of the differential ionization cross section is then given by:

$$\left.\frac{d\sigma_{ij}}{dE}\right|_g = \left(\frac{8\pi a_0^2 R^2}{mc^2\beta^2}\right)\left(\frac{1}{E}\right)\frac{df_j}{dE}\left[\ln\left(\frac{Q_j(E)}{Q_1(E)}\right) - \beta^2\right]. \tag{26}$$

The hard collision is considered to be a scattering of the fast electron by a free electron at rest. The expression for this differential cross section has been calculated by Bretagne *et al.* (1986):

$$\left.\frac{d\sigma_{ij}}{dE}\right|_{e-e} = \left.\frac{d\sigma_{ij}}{dE}\right|_h = \left(\frac{8\pi a_0^2 R^2}{mc^2\beta^2}\right)\left[\frac{1}{E^2} - \frac{1}{E(T + I_{ij} - E)}\left(\frac{mc^2(2T + mc^2)}{(T + mc^2)^2}\right) + \frac{1}{(T + I_{ij} - E)^2} + \frac{1}{(T + mc^2)^2}\right]. \tag{27}$$

Summing the glancing and hard components gives:

$$\frac{d\sigma_{ij}(T,E)}{dE} = \frac{8\pi a_0^2 R^2}{mc^2\beta^2}\frac{1}{E}\frac{df_j}{dE}\left[\ln\left(\frac{Q_j(E)2mc^2\beta^2}{E^2(1-\beta^2)}\right) - \beta^2\right] + N_j\left.\frac{d\sigma_{ij}}{dE}\right|_{e-e} \tag{28}$$

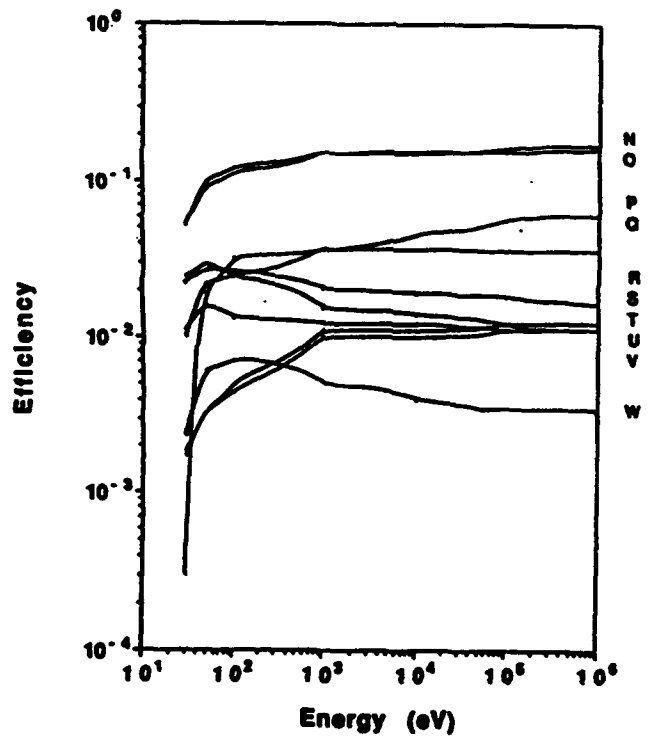

FIGURE 8. Deposition efficiencies of the $(3s^23p^4)$ $4s$ and $3d$ levels originating from the $J = 1/2$ level of the ground configuration $(3s^23p^5)$ of ArII as a fraction of the incident energy where the final states are as follows: $4s[^2P_{3/2}]$ (N); $4s[^2P_{1/2}]$ (O); $3d'[^2S_{3/2}]$ (P); $3d'[^2P_{1/2}]$ (Q); $3d[^2D_{3/2}]$ (R); $4s'[^2D_{3/2}]$ (S); $3d'[^2P_{3/2}]$ (T); $4s[^4P_{1/2}]$ (U); $4s[^4P_{3/2}]$ (V); $3d'[^2D_{3/2}]$ (W).

where N_j is the number of bound electrons in the jth shell and

$$\frac{df_j}{dE} = \frac{\sigma_{pj}}{4\pi\alpha a_0^2 R} \tag{29}$$

where σ_{pj} is the photoionization cross section of the jth shell and α is the fine structure coefficient. The term df_j/dE goes as $E^{-3.5}$ for large values of E (see Bretagne *et al.* 1986). It is assumed that the inner shells of singly ionized argon have the same energy dependence as those of neutral argon. Since df_j/dE decreases with increasing energy, an upper limit on its value can be set by calculating its value at the lower limit of energy, the ionization potential. This can be determined by using equation (29) and the value of the photoionization cross section at the ionization potential as given by Marr (1968).

The beam deposition efficiencies are defined as the fraction of the energy of the electron beam deposited in the gas by causing transitions from energy level i to k:

$$\eta_{ik}(T) = \frac{N_{ik}(T)E_{ik}}{T}. \tag{30}$$

Efficiencies are very useful in chemical kinetic models of REB produced plasmas and lasers. In particular, a pumping rate coefficient for raising ions in energy level i to a higher energy level k due to collisions with relativistic electrons can be defined as

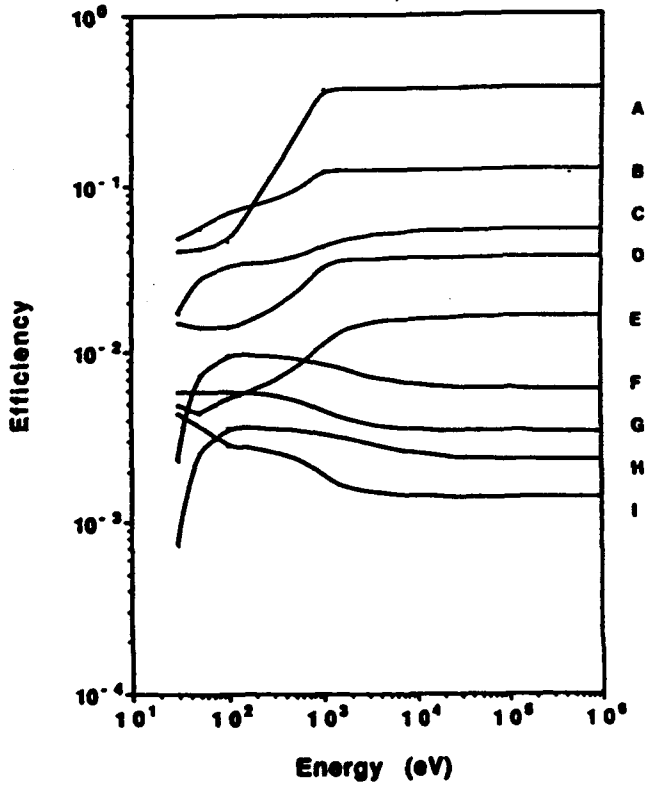

FIGURE 9. Deposition efficiencies of the $(3s^23p^4)$ $4p$ levels originating from the $J = 3/2$ level of the ground configuration $(3s^23p^5)$ of ArII as a fraction of the incident energy where the final states are as follows: $4p[^2P_{1/2}]$ (A); $4p[^2P_{3/2}]$ (B); $4p'[^2P_{3/2}]$ (C); $4p[^4D_{1/2}]$ (D); $4p[^4P_{3/2}]$ (E); $4p''[^2P_{3/2}]$ (F); $4p'[^2D_{5/2}]$ (G); $4p''[^2P_{1/2}]$ (H); $4p'[^2F_{7/2}]$ (I).

$$k_p(T) = \frac{J_b L_i(T) \eta_{ik}(T)}{eE_{ik}} \tag{31}$$

where J_b is the current density of the electron beam, $L_i(T)$ is the loss function for an electron with kinetic energy, T, incident on a target in energy level i, and E_{ik} is the energy of the transition.

Efficiencies for transition in ArII are displayed in figures 7–10. For most transitions the values of the efficiencies are roughly constant above a beam energy of 1 keV, although in a few cases η continues to increase up to beam electron energies of 10 keV. The results of these efficiency calculations will be used to model the plasma chemistry of argon gas excited and ionized by relativistic electrons (McGarrah & Brake 1990).

The efficiency for ionization can be considered by examining the extreme case of level i equal to the ground level and level k going to infinity. It would have a form analogous to that for excitation given in equation (30). Since the energy per ion pair is given by (T/N), which is equal to $(E_{ik}/\eta(T))$, where, for this case, N is the number of transitions from ground to infinity, i.e., the number of ionizations, and E_{ik} is simply the ionization potential. Energy per ion pair values for neutral argon are known to be fairly constant (Bekefi 1976). Since the ionization potential is constant, it is reasonable that the efficiency $\eta(T)$ should also be roughly constant. Ejection of inner shell electrons contributes approximately from 5% to as much as 12% of the transitions for electron energies higher than 10 keV. A few exceptions have lower contributions for inner shell electrons.

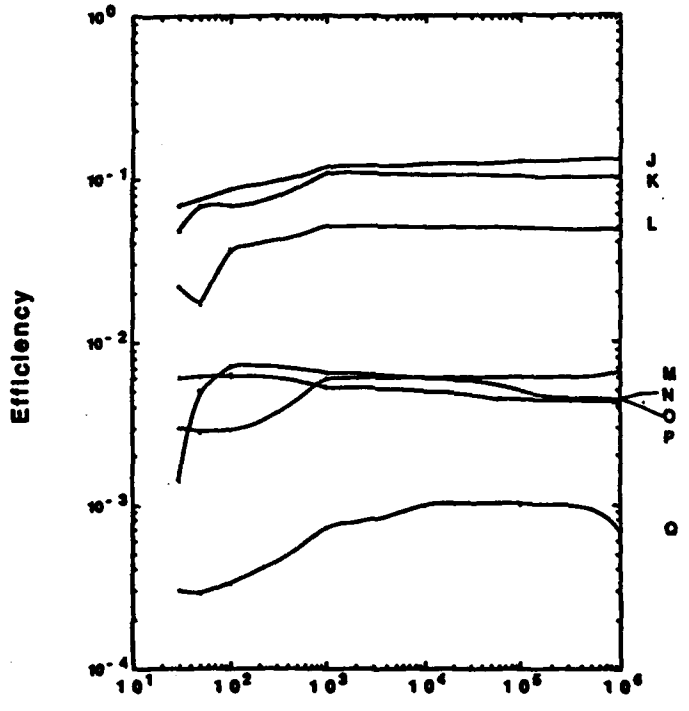

FIGURE 10. Deposition efficiencies of the $(3s^23p^4)\ 4p$ levels originating from the $J = 1/2$ level of the ground configuration $(3s^23p^5)$ of ArII as a fraction of the incident energy where the final states are as follows: $4p[^2P_{3/2}]$ (J); $4p[^2P_{1/2}]$ (K); $4p'[^2P_{3/2}]$ (L); $4p[^4D_{1/2}]$ (M); $4p''[^2P_{3/2}]$ (N); $4p'[^2D_{5/2}]$ (O); $4p''[^2P_{1/2}]$ (P); $4p[^4F_{3/2}]$ (Q).

4. Conclusions

A complete set of excitation cross sections has been generated for 69 allowed transitions in singly ionized argon. The generalized oscillator strength model for relativistic electrons was used. A modifier allowed for extension to lower energy electrons. A self-consistent set of oscillator dipole line strengths was generated for ArII by the Cowan code. When appropriate corrections were made it was possible to compare calculated cross sections with those measured in experiments starting with neutral argon. This analysis was performed for a $4s'$–$4p'$ transition measured by Feltsan and Povch (1970) and compared well with the experimental values. Efficiencies for populating excited states were calculated by using the method of Peterson and Green (1968) to quantify the effect of a beam electron and all subsequent generations of electrons produced. Results in most cases indicate that the efficiency is roughly constant above 1 keV. Inner shell ionization accounts for about 5 to 12% of the efficiency when considering electrons with energies greater than 10 keV.

Acknowledgments

We would like to express our gratitude to Robert D. Cowan for both the use of his code and a great deal of assistance and advice regarding its implementation. This project was supported in part by SDIO-IST.

REFERENCES

Bekefi, G. 1976 *Principles of Laser Plasmas* (John Wiley, New York).

Bethe, H. 1932 *Z. Physik*, **76**, 293.

Brake, M. 1986 *J. Appl. Phys.*, **60**, 99.

Brake, M. & Repetti, T. 1988 *IEEE Trans. on Plasma Sci.*, **16**, 581.

Bretagne, J. *et al.* 1986 *J. Phys. D: Appl. Phys.*, **19**, 761; 1986 *J. Phys. D: Appl. Phys.*, **19**, 779.

Book, D. 1983 *NRL Plasma Formulary* (Naval Research Laboratory, Washington, DC).

Cowan, R. D. 1981 *The Theory of Atomic Structure and Spectra* (University of California Press).

Feltsan, P. V. & Povch, M. M. 1970 *Optics and Spectroscopy*, XXVIII (2, p. 119).

Inokuti, M. 1971 *Rev. Mod. Phys.*, **43**, 297.

Marr, G. 1968 *Plasma Spectroscopy* (Elsevier, Amsterdam).

McGarrah, D. B. & Brake, M. L. 1990 *Laser and Particle Beams*, **8**, 507–520.

Moore, C. 1949 *Atomic Energy Levels: Derived from Analysis of Optical Spectra* (Circular of NBS no. 467, Department of the National Bureau of Standards).

Mott, N. F. & Massey, H. S. W. 1965 *The Theory of Atomic Collisions* (Oxford University Press, London).

Peterson, L. R. & Allen, J. E. Jr. 1971 *J. Chem. Phys.*, **56**, 6068.

Peterson, L. R. & Green, A. E. S. 1968 *J. Phys. B: At. Mol. Phys.*, **1**, 1131.

Werner, C. *et al.* 1977 *IEEE J. Quantum Electronics*, QE 13, 769.

Wiese, W. *et al.* 1969 *Atomic Transition Probabilities, Vol. II* (National Standard Reference Data Series, Number 22, National Bureau of Standards, Washington, DC).

Note added in proof

Varying α from 0.1 to 1.0 for an energy of 2 eV, typical of observed transitions, the term $\ln(2mc^2Cik/R)$ changes from 10.8 to 8.5 so the calculation is not sensitive to the value of α.

Laser and Particle Beams (1990), *vol.* 8, *no.* 3, *pp.* 507–520
Printed in the United States of America

Argon ion excitation by relativistic electrons: II. Chemical kinetics

By D. B. McGARRAH* AND M. L. BRAKE
Department of Nuclear Engineering, University of Michigan, Ann Arbor, MI 48109, USA

(Received 27 November 1989)

A model of an electron beam interacting with neutral argon was developed by solving the chemical kinetic rate equations for the time-dependent populations of ground and excited levels of ArI and ArII as well as the populations of electron energy groups. Intensities of spectral lines were calculated, from predicted population densities and Einstein coefficients, and compared to experimental results.

The thermal plasma is generated during the beam pulse and persists for some time after the pulse is terminated. Low energy levels of ArII with a 4*s* or 4*p* valence electron have similar time profiles to the plasma density. However, high energy levels of ArII with a 4*p*″ or 4*p*′ valence electron have similar temporal profiles as the beam current. They are populated predominantly by direct ionization and exceed levels populated by thermal electrons. The 4*p*″ levels decay rapidly to 4*s*″ levels, which have very high beam deposition efficiencies for being pumped back to the 4*p*″ levels. In this way, certain transitions such as 4*s*″–4*p*″ in ArII are pumped directly by the electron beam. Without direct ionization, these transitions would be negligible compared to those transitions which have lower energy levels.

1. Introduction

Plasmas produced by relativistic electron beams (REB) often emit large amounts of light (Wei *et al.* 1977). This property has allowed them to be successfully used as pump sources for gas lasers, particularly those utilizing atomic transitions in rare gases. Experiments performed at the Intense Beam Interaction Laboratory of the University of Michigan, searching for possible lasing lines in argon ions, observed unusual spectral emissions (Brake *et al.* 1986; Brake & Repetti 1988) that corresponded to transitions in ArII. The emissions that were unusually intense corresponded to transitions originating from high energy levels of ArII and indicated a larger population of certain energetic excited levels of ArII than would be indicated assuming a thermal distribution of excited level populations. A kinetic model of the plasma chemistry was needed that would include the effect of beam and cascade electrons as well as the thermal plasma and would not depend on assumption of particular equilibrium conditions in order to understand these unusually bright spectral lines.

2. Model

In the first paper of this series (McGarrah & Brake 1990), an "exact" calculation of the energy deposition from the beam was made in the sense that no thermal equilibrium conditions were required. As discussed in that paper, a *Continuously Slowing Down Approx-*

*D.B. McGarrah's current address is Sandia National Laboratories, Division 8233, Livermore, CA.

 0263-0346/90 $5.00 + .00

imation (CSDA) was utilized for calculation of the energy deposited in the gas due to the degradation of the beam and subsequent cascade electrons.

In this paper, the rate equations for the populations of ArI, ArI*, ArI(meta), ArII, ArII*, e_b, and e_{sec} will be derived, where

ArI	= ground level neutral argon,
ArII	= ground level singly ionized argon,
ArI*	= excited neutral argon,
ArI(meta)	= metastable neutral argon,
ArII*	= excited singly ionized argon,
e_b	= beam electrons,
e_{sec}	= secondary cascade electrons.

Although optically forbidden transitions generally occur with much lower probability than optically allowed transitions, there are certain metastable levels of ArI that are relatively long lived and can subsequently be ionized to form ArII. The population of metastable argon is expected to be quite small in comparison to that of the ground level neutral argon, but for completeness it will be included as a possible mechanism for producing the singly ionized argon (McGarrah 1989).

The spectral emissions of ArII observed in experiments (Brake *et al.* 1986; Brake & Repetti 1988) are identified as those corresponding to the transitions (Ne) $3s^23p^44s \rightarrow$ (Ne) $3s^23p^44p$ and (Ne) $3s^23p^43d \rightarrow$ (Ne) $3s^23p^44p$. Electron configurations with a principal quantum number above 4 were not included since no transitions from higher electron configurations were experimentally observed. Only optically allowed transitions were considered. The selection rules applied were:

$$\Delta L = \pm 1 \qquad \Delta J = 0, \pm 1 \tag{1}$$

where L is the magnitude of the orbital angular momentum of the ion and J is the magnitude of the total (orbital pulse spin) angular momentum. The selection rules also require

$$\Delta l = \pm 1 \tag{2}$$

for the electron in transition where l is the orbital angular momentum for the single electron.

The ground configuration of ArII ($1s^22s^23s^23p^5$) has odd parity, i.e., the sum of the angular momentum quantum numbers (l) for each electron is equal to an odd number. Therefore all energy levels reached from the first excitation must have even parity since parity is required to change during a transition. The energy levels—in Racah notation as given in Lengyel (1966)—included in the model are given in table 1.

Transitions from the ground configuration to (Ne) $3s^23p^44s$ or (Ne) $3s^23p^43d$ configurations with oscillator line strengths f_{ik} less than 0.01 are not used in the model since the stronger lines have values of f_{ik} on the order of 1.0. An exception to this is made only if an energy level is the lower level of a transition observed in the emission spectra. It may have a high transition probability of being reached by a three level system with an uppermost level which is more likely to be populated through a transition or series of transitions from the ground configuration of ArII or by direct excitation during the ionization of ArI.

The physical mechanisms included in the model for the populations of ArI and ArII were the following:

TABLE 1. Energy levels of ArII included in the model

Configuration	Term	J
a) Odd parity energy levels with ground level electron configuration		
$3s^23p^5$	$[^2P]$	3/2, 1/2
b) Even parity energy levels with excited electron configurations		
$3s^13p^6$	$[^2S]$	1/2
$3s^23p^4$ $(^3P)4s$	$[^4P]$	5/2, 3/2, 1/2
	$[^2P]$	3/2, 1/2
$(^1D)4s'$	$[^2D]$	3/2, 5/2
$(^1S)4s''$	$[^2S]$	1/2
$3s^23p^4$ $(^3P)3d$	$[^4D]$	5/2, 3/2, 1/2
	$[^4F]$	5/2, 3/2
	$[^2P]$	1/2, 3/2
	$[^4P]$	1/2, 3/2, 5/2
	$[^2F]$	5/2
$(^1D)3d'$	$[^2D]$	3/2, 5/2
	$[^2F]$	5/2
	$[^2P]$	3/2, 1/2
	$[^2S]$	1/2
$(^1S)3d''$	$[^2D]$	5/2, 3/2
c) Odd parity energy levels with excited electron configurations		
$3s^23p^4$ $(^3P)4p$	$[^4D]$	1/2
	$[^2P]$	1/2, 3/2
	$[^4P]$	3/2
$(^1D)4p'$	$[^2D]$	5/2
	$[^2F]$	7/2
	$[^2P]$	3/2
$3s^23p^4$ $(^1S)4p''$	$[^2P]$	1/2, 3/2

electron impact excitation: ArI and ArII can be excited from one energy level to a higher energy level due to inelastic scattering collisions with incident electrons.

radiative decay: Excited levels of ArI and ArII can spontaneously decay to lower energy levels.

electron impact ionization: ArI can be ionized by electron impact creating ArII.

radiative recombination: ArII can recombine with secondary electrons creating ArI and a photon.

three body recombination: ArII can recombine with secondary electrons in the presence of ArI.

The following assumptions were made to restrict the model:

a) All recombinations result in ground level neutral argon.

b) ArI that experience ionization produce ArII in either the first two energy levels, i.e., those with the (Ne) $3s^23p^5$ electron configuration or the excited energy levels with the (Ne) $3s^23p^44p$ electron configuration.

c) ArII ions that are produced in the two energy levels of the ground electron configuration are generated with respective probabilities $P1$ and $P2$ such that $P1 + P2 = 1$.

Since these two levels are so closely spaced, the distribution of ions created in each of these two energy levels were assumed to be in proportion to their degeneracies, i.e., $P_1 = \frac{2}{3}$ and $P_2 = \frac{1}{3}$.

d) Since the energy levels corresponding to the electron configuration (Ne) $3s^2 3p^4 4p$ are the highest energy configuration under consideration, these $4p$ levels will not experience excitation to higher levels nor will they have gain terms due to the higher levels decaying down to this configuration.

e) There is a small number, on the order of one percent, of neutral ArI atoms which ionize directly to ArII* in excited energy levels with the (Ne) $3s^2 3p^4 4p$ configuration.

3. Population rate equations

The rate equations for the population density of the lth energy level can be expressed in the general form:

$$\frac{dN(l)}{dt} = G - L \tag{3}$$

where G is the gain term and L is the loss term for $N(l)$, the population density of energy level l. Given the model and assumptions discussed in the previous section, the rate equations were written for the reactions shown in table 2.

The rate equation for neutral argon with the ground level electron configuration is:

$$\frac{dN_1(l)}{dt} = \sum_{k>1} A_1(k,l)N_1(k,t) - \left[\sum_{g_1=1}^{N_g} \sum_{g_2=g_1+1}^{N_g} \alpha(l,g_1,g_2)N_e(g_1,t)\right]N_1(l,t)$$
$$- \sum_{i<1} k_1(l,k)N_1(l,t) + \sum_{g=1}^{N_g}\left[\beta_r(g) + \beta_3(g)\sum_1 N_{II}(l,t)\right]N_e(g,t) \tag{4}$$

and the rate equation for levels of neutral argon with excited electron configurations is:

TABLE 2. Chemical reactions included in the model

1) Electron excitation of ArI:	$e + \text{ArI} \rightarrow \text{ArI}^* + e$
2) Electron ionization of ArI:	$e + \text{ArI} \rightarrow \text{ArII}(3p) + 2e$
3) Radiative decay of ArI:	$\text{ArI}^* \rightarrow \text{ArI} + h\nu$
4) Direct excitation of ArI:	$e + \text{ArI} \rightarrow \text{ArII}^*\ (4p) + 2e$
5) Electron excitation of ArII:	$e + \text{ArII} \rightarrow \text{ArII}^* + e$
	$e + \text{ArII}^* \rightarrow \text{ArII}^* + e$
6) Radiative decay of ArII:	$\text{ArII}^*(4p) \rightarrow \text{ArII}^* + h\nu$
	$\text{ArII}^* \rightarrow \text{ArII} + h\nu$
7) Radiative recombination:	$e + \text{ArII} \rightarrow \text{ArI} + h\nu$
	$e + \text{ArII}^* \rightarrow \text{ArI} + h\nu$
8) 3 body recombination:	$e + \text{ArII} + \text{ArI} \rightarrow \text{ArI} + \text{ArI}$
9) Creation of ArI(meta):	$e + \text{ArI} \rightarrow \text{Ar(meta)} + e$
10) Ionization of ArI(meta):	$e + \text{ArI(meta)} \rightarrow \text{ArII} + 2e$

$$\frac{dN_1(l)}{dt} = \sum_{i<1} k_1(i,l)N_1(i,t) - \left[\sum_{i<1} A_1(l,i) + \sum_{g_1=1}^{N_g}\sum_{g_2=g_1+1}^{N_g} \alpha(l,g_1,g_2)N_e(g_1,t)\right]N_1(l,t) \tag{5}$$

$k_1(i,k)$ is the pumping rate [sec^{-1}] for generating excitations from energy level i to energy level k in ArI due to electron impact excitation by the beam electrons and all secondary electrons with energy above the threshold E_{ik};

$A_1(k,i)$ is the Einstein A coefficient [sec^{-1}] for radiative decay from ArI in energy level k to ArI in energy level i due to the spontaneous emission of radiation;

$\alpha(l,g_1,g_2)$ is the ionization coefficient [cm^3/sec] for electrons in group g_1 causing an ionization of ArI in energy level l resulting in an emitted electron in energy group g_2;

$\beta_r(g)$ is the radiative recombination coefficient [cm^6/sec] for electrons in group g recombining with ArII to create ArI;

$\beta_3(g)$ is the three body recombination coefficient [cm^3/sec] for electrons in group g recombining with ArII to create ArI;

$N_e(g,t)$ is the number density [cm^{-3}] of electrons with kinetic energies in the interval ($T_g < T < T_{g-1}$) at time t; and

$N_1(l,t)$ is the number density [cm^{-3}] of ArI atoms in energy level l at time t.

The rate equation for the two ground levels of singly ionized argon is:

$$\begin{aligned}\frac{dN_1(l)}{dt} = {} & P(l)\sum_{l'=1}^{22}\sum_{g_1=1}^{N_g}\sum_{g_2=g_1+1}^{N_g} \alpha(l',g_l,g_2)N_e(g_1,t)N_1(l',t) \\ & - \sum_{k>1} k_{11}(l,k)N_{11}(l,t) - \sum_{g=1}^{N_g}\beta_r(g)N_e(g,t)N_{11}(l,t) \\ & + \sum_{k>1} A_{11}(k,l)N_{11}(k,t) - \sum_{g=1}^{N_g}\beta_3(g)N_e(g,t)\sum_{l'}N_1(l',t)N_{11}(l,t).\end{aligned} \tag{6}$$

The rate equation for levels of singly ionized argon with (Ne) $3s^23p^44s$ or (Ne) $3s^23p^43d$ electron configurations is:

$$\begin{aligned}\frac{dN_{11}(l,t)}{dt} = {} & \sum_{i<1} k_{11}(i,l)N_{11}(i,t) - \sum_{g=1}^{N_g}\left[\beta_r(g) + \beta_3(g)\sum_{l'=1}^{22}N_1(l',t)\right]N_e(g,t)N_{11}(l,t) \\ & - \left[\sum_{k>1} k_{11}(l,k) + \sum_{i<1} A_{11}(l,i)\right]N_{11}(l,t) + \sum_{k>1} A_{11}(k,l)N_{11}(k,t).\end{aligned} \tag{7}$$

The rate equation for levels of singly ionized argon with (Ne) $3s^23p^44p$ electron configuration is

$$\begin{aligned}\frac{dN_{11}(l,t)}{dt} = {} & \sum_{i<1} k_{11}(i,l)N_{11}(i,t) - \sum_{g=1}^{N_g}\left[\beta_r(g) + \beta_3(g)\sum_{l'=1}^{22}N_1(l',t)\right]N_e(g,t)N_{11}(l,t) \\ & - \sum_{i<1} A_{11}(l,i)N_{11}(l,t) + \sum_{l'=1}^{22}\sum_{g_1=1}^{N_g}\sum_{g_2=g_1+1}^{N_g} f(l)\alpha(l',g_1,g_2)N_e(g_1,t)N_1(l',t)\end{aligned} \tag{8}$$

where

$k_{II}(i,k)$ is the pumping rate [sec^{-1}] for generating excitations from energy level i to energy level k in ArII due to electron impact excitation by the beam electrons and all secondary electrons with energy above the threshold E_{ik};

$k_{therm}(i,k)$ is the pumping rate [sec^{-1}] for generating excitations from energy level i to energy level k in ArII due to electron impact excitation by the thermal electrons with energy above the threshold E_{ik};

$A_{II}(k,i)$ is the Einstein A coefficient [sec^{-1}] for radiative decay from ArII in energy level k to ArII in energy level i due to the spontaneous emission of radiation;

$N_{II}(l,t)$ is the number density [cm^{-3}] of ArII ions in energy level l at time t; and

$f(l)$ is the fraction of ArI directly ionized to the allowed $3s^23p^44p$ energy levels.

The pumping rates k_I, k_{II} [sec^{-1}] for exciting ArI and ArII from energy level i to energy level k are of the following form (Bretagne *et al.* 1988):

$$k_{ik}(T_b) = \frac{\eta_{ik}(T_b)L_i(T_b)}{E_{ik}} \frac{J_b}{|e|} \tag{9}$$

where $L_i(T_b)$ is the total loss function for an electron with kinetic energy T_b incident upon a target in energy level i, J_b is the current density of the electron beam, e is the charge of an electron, $\eta_{ik}(T_b)$ is the efficiency for an electron with kinetic energy T_b generating a transition in the target from energy level i to energy level k, and E_{ik} is the energy difference between levels k and i.

The ionization coefficients [sec^{-1}] are calculated similarly:

$$k_{ij}(T_b) = \frac{\eta_{ij}(T_b)L_i(T_b)}{I_{ij}} \frac{J_b}{|e|} \tag{10}$$

where $\eta_{ik}(T_b)$ is the efficiency for an electron with kinetic energy T_b generating an ionization in the jth shell of a target in energy level i, and I_{ij} is the ionization potential of the jth shell of a target in energy level i. $L_i(T_b)$, J_b, and e are defined the same as for (9).

The cascade electrons experience elastic electron-electron collisions which result in the thermalization of the electrons within each energy group. The time for this process to take place is on the order of a nanosecond. Since some electrons in energy bins below the inelastic threshold will be scattered elastically to energies above the threshold, their contribution must also be considered even though the actual elastic scattering will not be performed in the simulation. Boltzmann plots of selected experimentally measured intensities of spectral emissions, believed to be dominated by the plasma electrons, indicated an electron temperature of roughly 1.7 eV (Brake & Repetti 1988). This is also the temperature which characterizes the Maxwellian distribution that approximates the predicted distribution of electrons after elastic scattering. For each transition from energy level i to energy level k, an excitation rate will be calculated by evaluating the following at $T \simeq 1.7$ eV:

$$k_{thermal}(i,k) = n\langle\sigma_{ik}v\rangle = \int_{E_{ik}}^{E_u} F_{max}(k_BT)\sigma_{ik}(E = k_bT)v(E = k_bT)dE. \tag{11}$$

This thermal rate $k_{thermal}(i,k)$ in [sec^{-1}] was then added to the term $k(i,k)$ previously calculated for the rate of transitions created by the beam electron and secondary cascade electrons alone to give a total excitation rate.

It was also necessary to write rate equations for energy groups of secondary electrons since the recombination coefficients are functions of electron energy. The primary electrons

represent a special c
ergy, 300 keV in thi
current, the dimens

with $C_1 = 8.2 \times 10^1$
$\tau_3 = 300$ ns to mat
1988).

The energy bins fc
50, 20, 10, 5, 2, 1, 0
of the calculated dis
tron from ground le
gies over 200 eV w
electrons with kinet
the secondary electrc
ing collisions) that s
suffer scattering col
lower energy bin as
ion.

The rate equation

$$\frac{dN_e(g,t)}{dt}$$

where α and β are th
rate [cm^3 sec^{-1}] of

which can be rewrit

by making the follc

represent a special case of electrons all with kinetic energy equal to the beam electron energy, 300 keV in this case. The beam electron rate equation is deduced from the measured current, the dimensions of the cathode, and the energy of the beam where

$$\frac{dN_{eb}(l,t)}{dt} = \begin{cases} C_1 & t < \tau_1 \\ 0 & \tau_1 \le t < \tau_2 \\ -C_2 & \tau_2 \le t < \tau_3 \\ 0 & t > \tau_3 \end{cases} \tag{12}$$

with $C_1 = 8.2 \times 10^{17}[\text{cm}^{-3}\,\text{s}^{-1}]$, $C_2 = 2.7 \times 10^{17}[\text{cm}^{-3}\,\text{s}^{-1}]$, $\tau_1 = 25$ ns, $\tau_2 = 225$ ns, and $\tau_3 = 300$ ns to match the experimental conditions (Brake *et al.* 1986; Brake & Repetti 1988).

The energy bins for secondary electrons encompassed electrons with energies of 200, 100, 50, 20, 10, 5, 2, 1, 0.5, 0.2, and 0.1 eV. The upper limit was chosen from the examination of the calculated distribution of secondary electrons after one ionization of a valence electron from ground level neutral argon. The number of secondary electrons with kinetic energies over 200 eV was negligible. An energy bin "g" is defined such that it contains all electrons with kinetic energies $T_g < T < T_{g-1}$. The gain term for any given energy bin in the secondary electron rate equation is due to electrons of higher energy (created from ionizing collisions) that scatter down into the energy bin. The loss term is due to electrons which suffer scattering collisions which cause them to lose sufficient energy to drop down to a lower energy bin as well as electrons in the bin which experience recombination with an ArII ion.

The rate equation for secondary electrons of group g is given by the following expression:

$$\begin{aligned} \frac{dN_e(g,t)}{dt} = & \sum_{l=1}^{22} \sum_{G_1=1}^{g-1} \alpha(l,G_1,g) N_l(l,t) N_e(G_1,t) \\ & + \sum_{G_2=2}^{g-1} \sum_{l=1}^{22} \chi(l,G_2,g) N_l(l,t) N_e(G_1,t) \\ & - \sum_{G_2=g}^{N_g} \sum_{l=1}^{22} \chi(l,2,G_2) N_l(l,t) N_e(g,t) \\ & - \left[\beta_r(g) + \beta_3(g) \sum_{l'=1}^{22} N_l(l',t)\right] N_e(g,t) \sum_{l=1}^{22} N_{ll}(l,t) \end{aligned} \tag{13}$$

where α and β are the ionization and recombination coefficients, as previously defined. The rate [cm^3 sec^{-1}] of creation of electrons due to ionization is calculated as follows:

$$\alpha(T_g) = \sigma_{\text{ion}}(T_g) v_g \tag{14}$$

which can be rewritten as

$$\alpha(T_g) = v_g \int \frac{d\sigma_{\text{ion}}(T_g,E)}{dE}\, dE \tag{15}$$

by making the following approximation

$$\int \frac{d\sigma_{\text{ion}}(T_g,E)}{dE}\, dE \approx \frac{\int E \dfrac{d\sigma_{\text{ion}}(T_g,E)}{dE}\, dE}{\int dE} \tag{16}$$

and using the definition of the loss function given in McGarrah & Brake (1990), the ionization coefficient can be expressed as

$$\alpha(T_g) = \frac{L_{\text{ion}}(T_g)v_g}{\Delta E}. \tag{17}$$

The scattering coefficients $\chi(l, g_1, g_2)$ [$\text{cm}^3\,\text{sec}^{-1}$] represent the rate at which electrons experience scattering collisions, namely, excitation or ionization, that result in electrons having energy characteristics of one energy group to an energy within the interval of a lower energy group. The scattering (excitation and ionization) coefficient can be determined using the total, as opposed to ionization, loss function.

$$\chi(T_g) = \frac{L_{\text{TOT}}(T_g)v_g}{\Delta E} \tag{18}$$

where for energy group g, in both cases,

$$\Delta E = T_{g-1} - T_g. \tag{19}$$

The series of coupled rate equations was solved using a software package of FORTRAN codes created at Lawrence Livermore Laboratory known as EPISODE (experimental package for integration of systems of ordinary differential equations, see Hindmarsh and Byrne (1975)).

4. Results

The electron density can be obtained by summing each of the calculated secondary electron energy groups $N_e(g, t)$ over all g. The result of these calculations at a pressure of 50 Torr is shown in figure 1. The plasma density is roughly linear over the period of the beam pulse and then remains constant. This behavior is in agreement with literature (Miller 1982) which indicates that the partial time derivative of the plasma density due to the beam elec-

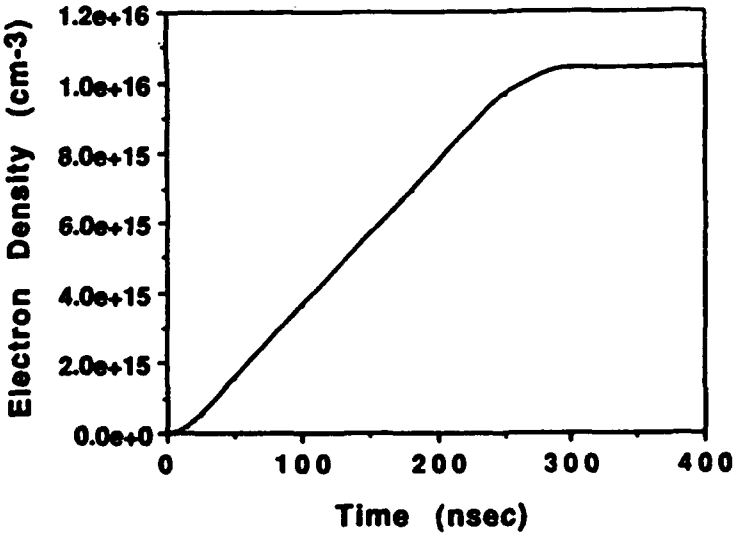

FIGURE 1. Plasma density versus time at pressure equal to 50 Torr.

trons is proportional to
for 200 nanoseconds, s
will eventually decreas
was calculated for pr
Figure 2 shows the
the visible range as pr
cause they all have (N
tion is indicated in ta
Three of the line in
emissions have upper
ble 3), i.e., they are
indicate that these pe
valence electrons. Th
must satisfy the select

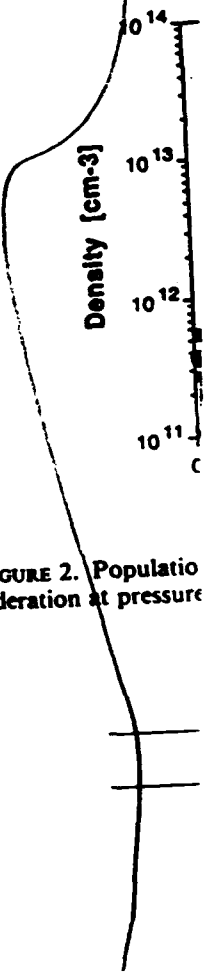

FIGURE 2. Populatio
sideration at pressure

trons is proportional to the beam electron density. In this case the beam density is constant for 200 nanoseconds, suggesting a linear time dependence for the plasma density. This value will eventually decrease due to recombination long after the beam pulse. Similar behavior was calculated for pressures up to 750 Torr with peak density of 1.7×10^{17} cm^{-3}.

Figure 2 shows the time dependent populations of 9 upper levels of the 10 transitions in the visible range as predicted by the simulation. They are labeled $4p(1)$ through $4p(9)$ because they all have (Ne) $3s^2 3p^4 4p$ electron configuration. The remainder of their designation is indicated in table 3.

Three of the line intensities were dramatically larger than the other seven. These three emissions have upper levels with $4p'$ and $4p''$ valence electrons (levels 7, 8, and 9 of table 3), i.e., they are among the highest energy levels observed. A thermal model would indicate that these populations should be small relative to the less energetic levels with $4p$ valence electrons. The mechanism of direct ionization indicated by Reaction (4) in table 2 must satisfy the selection rules (Koozekanani 1966) of equations (1) and (2); therefore it can

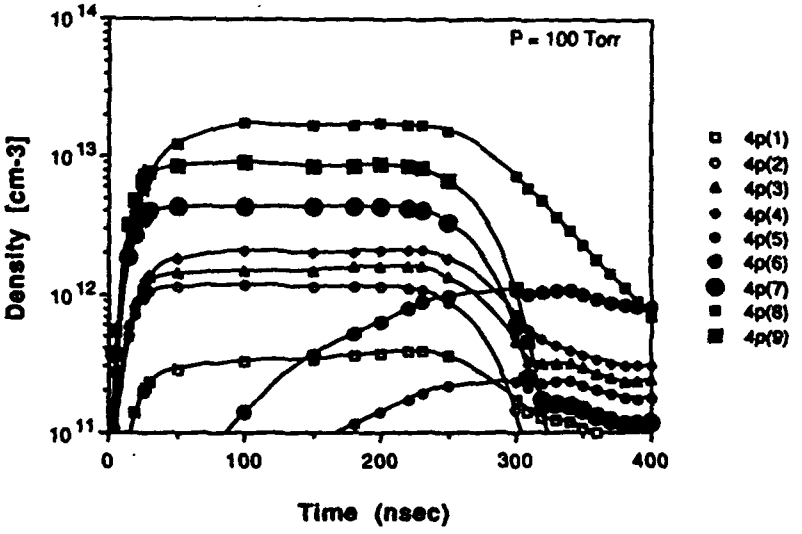

FIGURE 2. Populations of the nine (Ne) $3s^2 3p^4 4p$ excited electron energy levels of ArII under consideration at pressure equal to 100 Torr. See table 3 for level configuration.

TABLE 3. Identification of energy levels for figure 2

Label	Configuration-Term	J
$4p(1)$	$3s^2 3p^4\ (^3P)4p\ [^4D]$	1/2
$4p(2)$	$(^3P)4p\ [^2P]$	1/2
$4p(3)$	$(^3P)4p\ [^2P]$	3/2
$4p(4)$	$(^3P)4p\ [^4P]$	3/2
$4p(5)$	$(^1D)4p'\ [^2D]$	5/2
$4p(6)$	$(^1D)4p'\ [^2F]$	7/2
$4p(7)$	$(^1D)4p'\ [^2P]$	3/2
$4p(8)$	$(^1S)4p''\ [^2P]$	1/2
$4p(9)$	$(^1S)4p''\ [^2P]$	3/2

only contribute to the populations of the low energy $4p(1)$ through $4p(4)$ levels and the $4p'$ level with $J = \frac{3}{2}$ (i.e., $4p(7)$) and the two $4p''$ levels ($4p(8)$ and $4p(9)$). Due to this direct ionization, the two $4p''$ energy levels and the $4p'[^2P_{3/2}]$ energy level are substantially larger than the other energy levels and appear to rise sharply with the incidence of the electron beam. They remain flat while the beam pulse is constant and rapidly decline as it is turned off. The smallest populations, corresponding to lower energy levels, increase slowly with time or remain roughly constant even after the beam pulse. This is similar to the time dependence of the plasma electron density.

The time-dependent populations of the upper levels were used to generate relative inten-

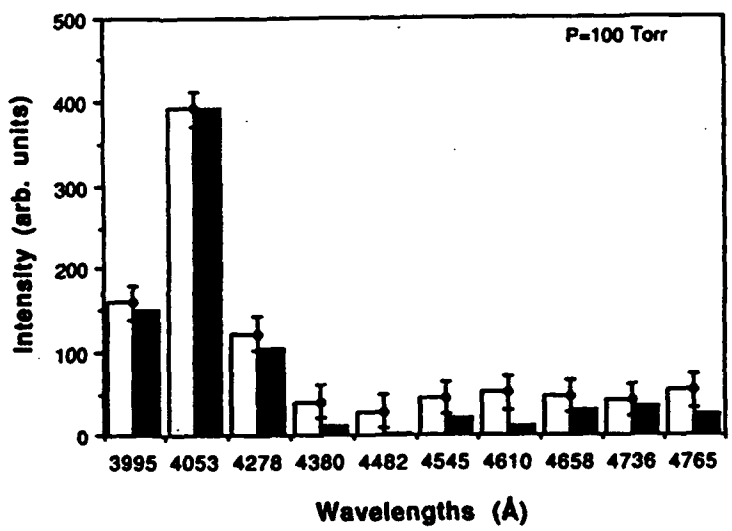

FIGURE 3a. Comparison of normalized calculated intensities (solid boxes) with measured values (open boxes) for 10 experimentally observed wavelengths at 100 Torr.

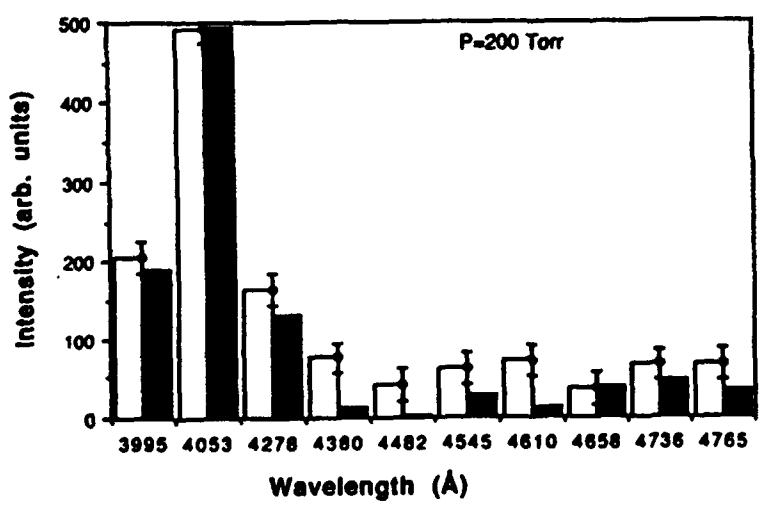

FIGURE 3b. Comparison of normalized calculated intensities (solid boxes) with measured values (open boxes) for 10 experimentally observed wavelengths at 200 Torr.

sity values so that they could be compared to experimental results obtained from an intense, relativistic electron beam (300 keV, 1kA, 300 ns) injected into a vacuum vessel which was back filled with argon at pressures ranging from 1 to 750 Torr (Brake *et al.* 1986; Brake & Repetti 1988). Since relative rather than absolute intensities were measured in the experiment, the model intensities were scaled to the experimentally observed intensities by normalizing them to the 4053 Å line.

The results for pressures from 100 Torr to 750 Torr are given in figure 3a–3d and show

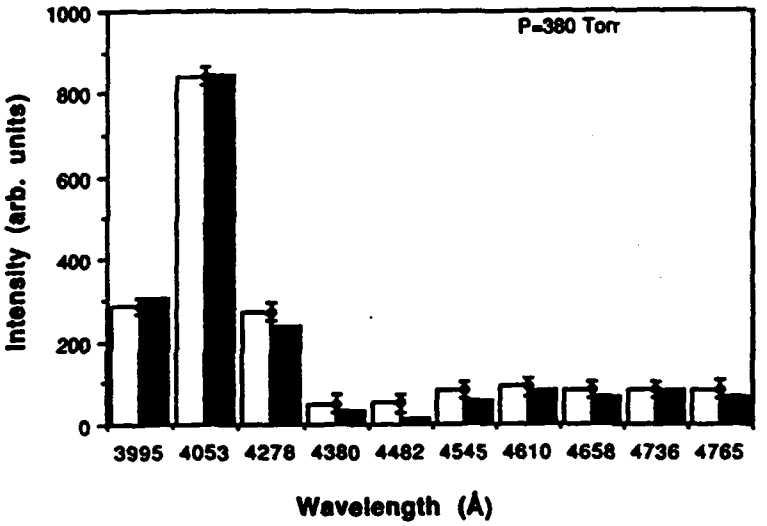

FIGURE 3c. Comparison of normalized calculated intensities (solid boxes) with measured values (open boxes) for 10 experimentally observed wavelengths at 380 Torr.

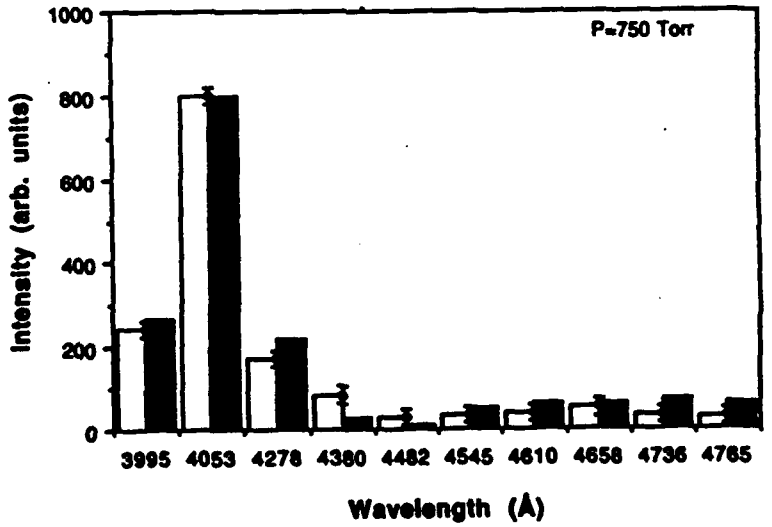

FIGURE 3d. Comparison of normalized calculated intensities (solid boxes) with measured values (open boxes) for 10 experimentally observed wavelengths at 750 Torr.

excellent agreement. In figure 4a and 4b the calculated ratio of the intensity of the 4053 Å line to the two other enhanced lines at 3995 Å and 4278 Å were compared to the experimentally observed values over a range of pressures. The calculated values agree extremely well with measured values and also support the concept that these lines are dominated by beam electron densities, constant over pressure, and ArII densities, linear with pressure. If all three intensities are linear in pressure, their ratios will then be constant with pressure. The intensities of the three lines at 3995, 4053, and 4278 Å are presented as a function of pressure in figure 5. The calculated values are indeed linear with pressure. The experimental values concur at low pressures but begin to diminish at higher pressures where the analytical assumption of an optically thin plasma may begin to break down.

The high energy $4p''$ and $4p'[_2P^{3/2}]$ energy levels can be reached due to direct ionization of neutral argon in the ground level. This is possible because the transition from ArI

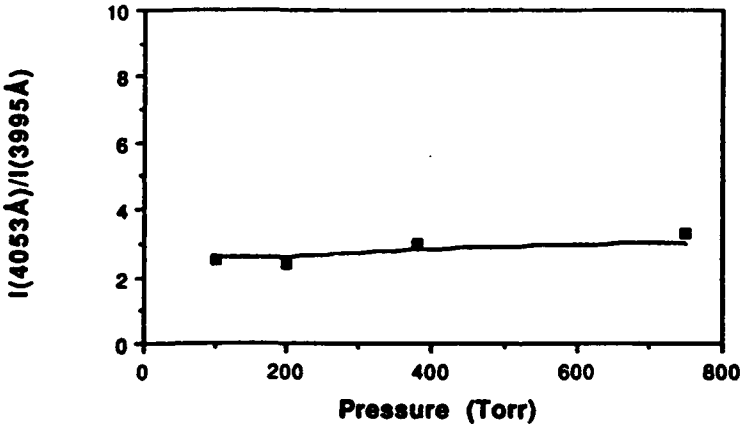

FIGURE 4a. Comparison of the calculated (solid line) and measured ratios of the normalized intensity for the 4053 Å to the 3995 Å line.

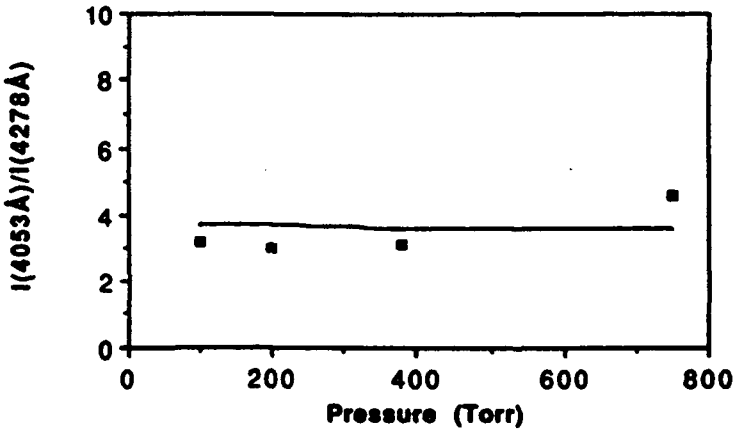

FIGURE 4b. Comparison of the calculated (solid line) and measured ratios of the normalized intensity for the 4053 Å line to the 4278 Å line.

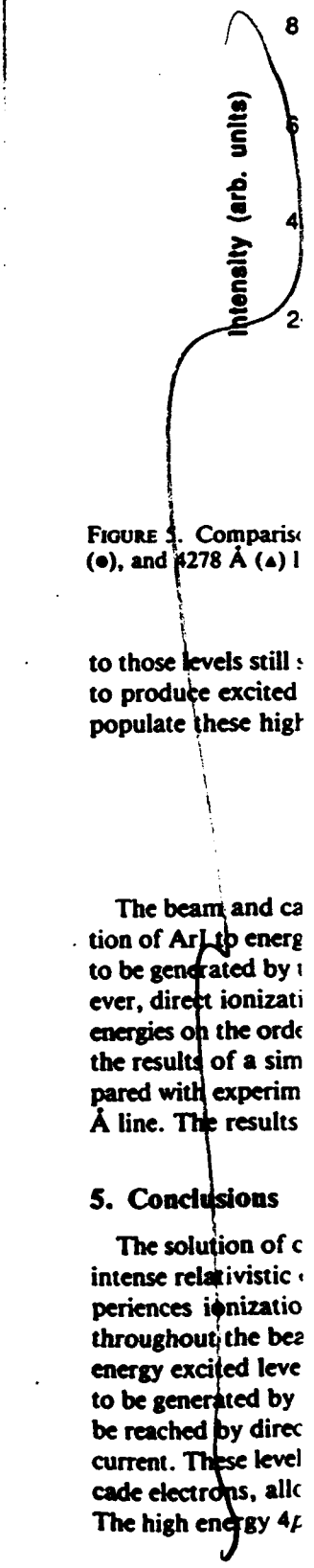

FIGURE 5. Comparis
(●), and 4278 Å (▲) l

to those levels still
to produce excited
populate these high

The beam and ca
tion of ArI to energ
to be generated by
ever, direct ionizati
energies on the orde
the results of a sim
pared with experim
Å line. The results

5. Conclusions

The solution of c
intense relativistic
periences ionizatio
throughout the bea
energy excited leve
to be generated by
be reached by direc
current. These level
cade electrons, allc
The high energy $4p$

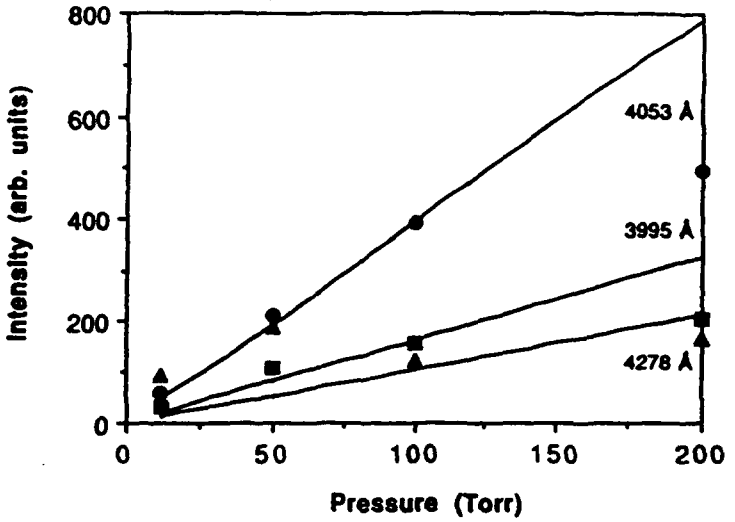

FIGURE 5. Comparison of calculated (solid line) and experimental intensities of 3995 Å (■), 4053 Å (●), and 4278 Å (▲) lines versus pressure.

to those levels still satisfies equation (1). Although only about 1% of ionization is believed to produce excited energy levels (Bennett *et al.* 1966), this still provides a mechanism to populate these high energy levels which will dominate over the three step procedure:

$$e + \mathrm{ArI} \rightarrow \mathrm{ArII}(3p) + 2e \tag{20a}$$

$$e + \mathrm{ArII}(3p) \rightarrow \mathrm{ArII}(4s,3d) + e \tag{20b}$$

$$e + \mathrm{ArII}(4s,3d) \rightarrow \mathrm{ArII}(4p) + e. \tag{20c}$$

The beam and cascade electrons are able to drive this process because the direct ionization of ArI to energetic ArII* represents a transition of over 30 eV and is therefore unlikely to be generated by the thermal electrons characterized by an energy of less than 2 eV. However, direct ionization would be a more probable transition for the cascade electrons with energies on the order of 100 eV. The significance of this effect is indicated by figure 6, where the results of a simulation performed without the inclusion of direct ionization are compared with experimental intensities for the 10 observed transitions, again scaled to the 4053 Å line. The results are seen to differ dramatically.

5. Conclusions

The solution of coupled differential rate equations describing the chemical kinetics of an intense relativistic electron beam interacting with neutral argon indicates that the gas experiences ionization of about 1% of the argon. The plasma density increases linearly throughout the beam pulse and remains for some time after the beam is turned off. Low energy excited levels of ArII have time profiles similar to the plasma density and appear to be generated by the thermal electrons. High energy $4p''$ levels and the $4p'$ level that can be reached by direct ionization of ArI have the same temporal profile as the electron beam current. These levels are populated almost entirely by direct ionization by the beam and cascade electrons, allowing them to be more densely populated than the lower energy levels. The high energy $4p''$ levels then have a large Einstein A coefficient for decaying to $4s''$ en-

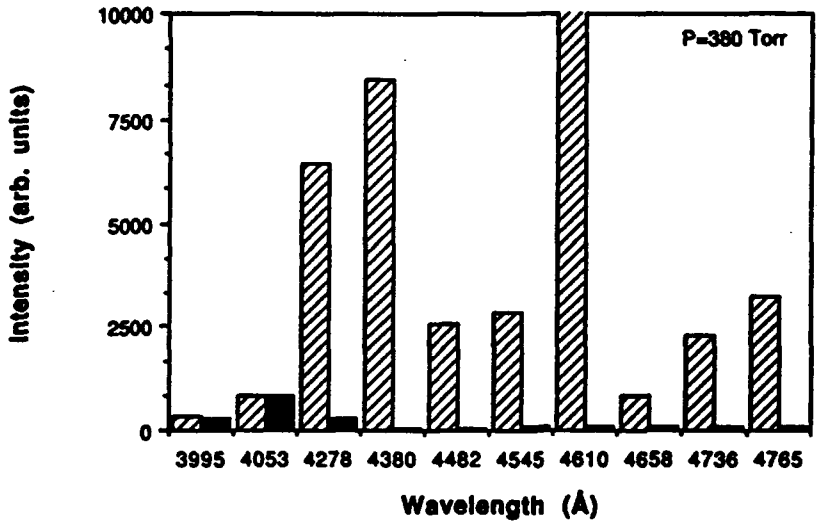

FIGURE 6. Predicted relative intensities (dashed box) for a simulation which does not include direct excitation from ArI to 4p levels of ArII compared with the experimental values (solid box).

ergy levels, which in turn have high beam deposition efficiencies for being pumped by the electron beam back up to the $4p''$ levels. In this way certain transitions between energetic excited levels of ArII are pumped by the electron beam. These transitions between high energy excited levels would be negligible if the mechanism of direct ionization was not considered. The model achieved excellent agreement with the experimental measurements of relative intensities of spectral emissions from argon ions over a range of pressures from 50 to 750 Torr and should prove useful for other studies of beam pumped rare gases.

Acknowledgment

This project was supported in part by SDIO-IST.

REFERENCES

BENNETT, W. R. JR. *et al.* 1966 *Phys. Rev. Letters*, **17**, 987.
BRAKE, M. *et al.* 1986 *J. Appl. Phys.*, **60**, 99.
BRAKE, M. & REPETTI, T. 1988 *IEEE Trans. on Plasma Sci.*, **16**, 581.
BRETAGNE, J. *et al.* 1986 *J. Phys. D: Appl. Phys.*, **19**, 779; 1986 *J. Phys. D: Appl. Phys.*, **19**, 793.
HINDMARSH, A. C. & BYRNE, G. D. 1975 *UCID-30112* (Lawrence Livermore Laboratory, California).
KOOZEKANANI, S. H. 1966 *IEEE J. Quant. Electr.*, QE-2, 770.
LENGYEL, B. A. 1966 *Introduction to Laser Physics* (John Wiley, New York).
MCGARRAH, D. B. 1989 *Ph.D. thesis* (University of Michigan, Ann Arbor).
MCGARRAH, D. B. & BRAKE, M. L. 1990 *Laser and Particle Beams*, **8**, 493–506.
MILLER, R. B. 1982 *Intense Charged Particle Beams* (Plenum Press, New York, p. 194).
WEI, P. S. P., ADAMSKI, J. L. & BEYMER, J. R. 1977 *J. Appl. Phys.*, **48**, 568.